High fidelity operations in a europium doped inorganic crystal

Pernilla Helmer

A thesis presented for the degree of Bachelor of Physics

LUND
UNIVERSITY

Supervised by Adam Nilsson and Prof. Stefan Kröll

Division of Atomic physics

Department of Physics

Lund University

January 2015

Abstract

The computer has since it was invented become a most crucial tool for scientists in all fields. It has however severe limitations when it comes to e.g. simulating quantum systems, a task quantum computers might be able to perform. In this project the possibility to create quantum hardware with the inorganic crystal Y_2SiO_5 doped with triply charged europium of isotope 151, $^{151}Eu^{3+}$ has been investigated. The ground level of Eu, which is a rare-earth element, is denoted $^7F_0$ and consists of three hyperfine levels. These have lifetimes of several days at cryogenic temperatures, and the Eu-ions could therefore be used as semi-permanent quantum memory.The aim was to create a prototype qubit, in analogy to a classical bit, and to obtain as high transition fidelity as possible between the two qubit states $|0\rangle$ and $|1\rangle$.

Transitions between two of the ground levels and one excited level were used for the two qubit states $|0\rangle$ and $|1\rangle$. All ions experience a different crystal field, and thus their transitions are all differently shifted. Any ion with undesired transitions close to the selected frequencies were therefore moved to an auxiliary ground state using spectral hole burning.

The aim of the present work was to achieve more than 99% transfer efficiency for $^{151}Eu^{3+}$ in agreement with simulations. The results were consistently lower than expected, and no transfer efficiency above 98.4% was attained. This could be explained by flaws in the setup, and successful results are still to hope for.

Acknowledgments

I would like to thank my supervisor Adam Nilsson for all his help, for patiently explaining everything to me also when I came to ask about it the third time as I hadn't understood it properly the two first times and for pretty much always being available. I'd also like to thank Lars Rippe and Andreas Walter for senior advise regarding the setup and for answering questions when Adam by some reason was not present, or didn't know the answer to my question. And of course I want to thank my second supervisor Stefan Kröll who offered me this project.

I would besides these persons like to thank my scout leader, who entertained me on a long train ride with quantum mechanics, and initialized my interest for the subject, and Mattias Nilsson who I've never met, but who wrote a very neat PhD thesis from which I have gathered most of the theory for this bachelor's thesis [1].

Acronyms

RE	-	rare earth element
RE-crystal	-	rare-earth-ion-doped inorganic crystal
YSO	-	Y_2SiO_5, Yttrium Orthosilicate
Eu	-	europium
Pr	-	praseodymium
AOM	-	acusto-optic modulator
FWHM	-	full width half maximum

Contents

1 Introduction

In today's society the computer has become an increasingly important device, and the development of this device is continuously in progress. The computer has, as a fruit of science, opened amazing possibilities for scientists in all fields.

Something that physicists have come to wish for is a computer that can accurately simulate a quantum system. This is with today's technology only possible for a few body systems, as very complex equations are required to make these simulations accurately. Another limitation of the classical computer is that it cannot generate true random numbers. Thus there are needs for a more powerful type of computer: the quantum computer.

In this project the possibility of creating a qubit, which is the quantum analogy to a bit, in a rare-earth-ion-doped inorganic crystal was investigated. To be able to use the qubit for actual calculations operations need to be possible to do with very high fidelity. In this project, this was analogous to make high efficiency transfers between different ionic states.

How the qubit and the quantum computer works is described in section 1.1 and 1.2. To implement the theory presented in these sections in the real world is far from trivial. The Rare-earth-elements are commonly used in quantum information because they have several properties that are suitable for this implementation. How these properties are used for designing a qubit is explained in section 1.3 and 1.4.

1.1 The Quantum Computer

A universal quantum computer is a computer which can "perfectly simulate any finite, realizable physical system" [2]. It could do anything a classical computer could do, but it could also perform tasks that have no classical analogue. As mentioned it would for example be able to generate true random numbers. Although not necessarily more efficient for all types of problem, it would be much better at solving some kinds of problems due to the quantum nature of the system.

The processing unit of a quantum computer is called a qubit (quantum bit), in analogy to a classical bit. A classical bit can take one of the two discrete values 0 and 1, and this causes several limitations on the classical computer. When executing a computation, the computing machine is first prepared in some initial state which is changed by dynamical processes to end up in a final state. The classical computer has a physical limitation when performing computations as it is discrete. This causes the classical computer to be deterministic, which means that the output will be fully determined by the initial state and the computation. From this follows for example that the classical computer can not handle a continuum, but merely approximate it [2], nor can it generate true randomness. These are both features the quantum computer would have.

The qubit consists of a two level quantum system, where the two eigenstates are called $|0\rangle$ and $|1\rangle$. The qubit can be in either state $|0\rangle$ or state $|1\rangle$, in correspondence to the values 0 and 1 for a bit. It can also be in a superposition of the two states, $\alpha|0\rangle + \beta|1\rangle$. The properties of a two level quantum system is further explained in section 1.2. Upon readout of a superposition state the qubit wavefunction will collapse to one of the two states with probabilities given by the input and the computation. The readout of a single computation will thus not be deterministic.

The possibility of putting the qubit in a superposition state leads to another advantage with the quantum computer, called quantum parallelism. This means that a single quantum processing unit can carry out multiple computations simultaneously, as the quantum system can be in a superposition of several states. A problem though is the readout of such a system: As mentioned the readout of a superposition state will cause the wave functions to collapse, and only one of all possible results can be obtained from each computation, and a lot of information is lost.

As the output is not deterministic, the computation could be carried out N times to obtain N answers. For large enough N this should approximately give the probability amplitudes for the superposition state, and thus approximately all information about the system after the computation. Then, however, the idea of quantum parallelism is somewhat lost as only one answer per processing unit is accessible for each computation.

Instead of carrying out the calculation N times, the algorithm for computing the calculation could be very intelligently designed. There are examples of algorithms making use of the quantum parallelism, such as the Deutsch-Jozsa algorithm proposed in 1992 [3].

1.1.1 The quantum NOT-gate

The purpose of the present work was to create a prototype qubit, more specifically a NOT-gate. The classical NOT-gate is a negating logical gate, which means that it changes the input to the logical opposite. In other words it changes a 0 into a 1 and a 1 into a 0. The quantum NOT-gate would then invert the input: $\alpha|0\rangle + \beta|1\rangle \rightarrow \alpha|1\rangle + \beta|0\rangle$.

To create the quantum NOT-gate is however not trivial, but rather complicated. The ground level of the europium ion is split into three hyperfine levels. Life times of several days can be achieved for these levels, and this could be used for creating the prototype qubit. In figure 1.1a two of the ground levels has been denoted $|0\rangle$ and $|1\rangle$ respectively. The third ground level has been denoted $|\text{aux}\rangle$ which is the auxiliary level. This level will be used for storage of undesired ions, as will be explained further in section 1.4. The ions are moved between the $|0\rangle$ and $|1\rangle$ states via an exited state, $|e\rangle$, using laser pulses. These transitions are indicated by the arrows. The ions are not moved directly between the two ground states, as the energy difference between them is to small for direct manipulation with optical frequencies.

In figure 1.1b-d it is shown how the NOT-gate is implemented in the europium ion. For each figure one step in the procedure is taken, and the complete operation will be:

$$\begin{aligned} &\alpha\,|0\rangle + \beta\,|1\rangle \rightarrow \\ &\alpha\,|e\rangle + \beta\,|1\rangle \rightarrow \\ &\alpha\,|1\rangle + \beta\,|e\rangle \rightarrow \\ &\alpha\,|1\rangle + \beta\,|0\rangle \end{aligned} \tag{1.1}$$

This procedure does however use three different states, and the described qubit consists of two coupled two level systems instead of just one, namely $|0\rangle \leftrightarrow |e\rangle$ and $|1\rangle \leftrightarrow |e\rangle$.

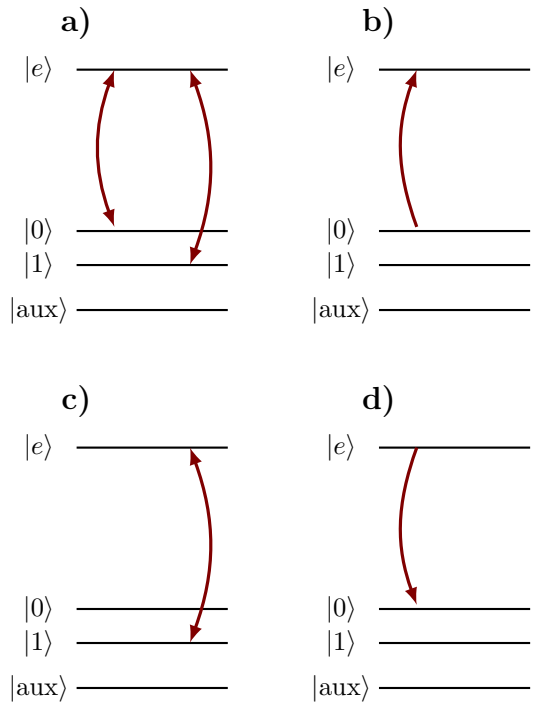

Figure 1.1: *The procedure of a NOT-gate implemented in the europium ion. In a) the transitions that were used for creating the gate is indicated. In b)-d) the successive procedure of inverting the superposition state is shown. In b) the $|0\rangle$ part is transferred into $|e\rangle$. In c) $|1\rangle$ and $|e\rangle$ are inverted, and in d) the part which is now in $|e\rangle$ is transferred down into $|0\rangle$. This completely inverts the initial superposition state, as shown in equation 1.1.*

1.2 Two Level Quantum Systems

The simplest quantum system is one with only two eigenstates. In nature no system is this simple, but the two level quantum system can still be useful for describing quantum phenomena. For example, the two level system is very useful for describing how a quantum system reacts to a laser pulse, as the laser is only resonant with one transition at a time.

The two eigenstates of the two level quantum system is here denoted $|g\rangle$ and $|e\rangle$ for ground and excited state. The complete system can be either in one of the eigenstates, or in a superposition of the two. Any of these states are pure quantum states. The system can be described by a vector in a unit sphere, the so called Bloch sphere, with the axes denoted u, v and w. The w-axis represents the inversion of the state (see equation 1.3b). Figure 1.2a describes the eigenstate $|g\rangle$ with $w = -1$. If the system is instead in the eigenstate $|e\rangle$, $w = 1$. Any other value of w represents a superposition state Ψ:

$$|\Psi(t)\rangle = c_g(t)\,|g\rangle + c_e(t)\cdot e^{-i\omega_r t}\,|e\rangle \tag{1.2}$$

with $|c_g(t)|^2$ and $|c_e(t)|^2$ being time dependent probability amplitudes satisfying the relation $|c_g(t)|^2 = |\langle g\,|\,\Psi(t)\rangle|^2$, $|c_e(t)|^2 = |\langle e\,|\,\Psi(t)\rangle|^2$ and $\langle\Psi(t)\,|\,\Psi(t)\rangle = |c_e(t)|^2 + |c_g(t)|^2 = 1$. The factor $e^{-i\omega_r t}$ describes the relative phase between the two states, which is described by the $u-$ and $v-$vectors. The quantity ω_r is the resonance frequency of the system, given as $\omega_r = (E_e - E_g)/\hbar$. Here E_g and E_e are the energies of the two states, respectively, and $\hbar$ is the Planck constant. Figure 1.2b illustrates a superposition state in the Bloch sphere.

The relation between u, v and w is described as follows [1]:

$$u(t) - iv(t) = 2\cdot c_e(t)\cdot c_g^\star(t) \tag{1.3a}$$

$$w(t) = |c_g(t)|^2 - |c_e(t)|^2 \tag{1.3b}$$

As discussed above, w describes the inversion, that is the probability of finding the atom in the excited

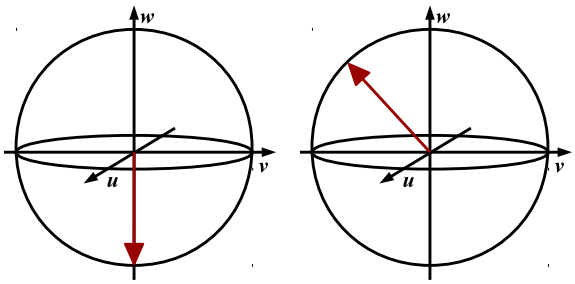

Figure 1.2: *a) The figure shows a vector* $\mathbf{V}$ *in the Bloch sphere, describing the eigenstate* $|g\rangle$ *in a two level quantum system with* $w = -1$*. b) Here the vector* $\mathbf{V}$ *in the Bloch sphere describes one of infinitely many superpositions of the two states* $|g\rangle$ *and* $|e\rangle$*.*

state compared to finding it in the ground state. u and v express the phase, or the oscillations at the resonance frequency, ω_r. If an electric field oscillating at ω_r is applied to the system, the $u-$component will describe the part oscillating in phase with the field (or completely out of phase in case u is negative), and the $v-$component will describe the part 90° out of phase.

For a pure state the vector always has the length 1, and the state is described by some point on the surface of the sphere. This is illustrated in figure 1.2. Any point within the sphere corresponds to a mixed state. Whenever the quantum system is interacting with the environment in an uncontrolled way, the states will be mixed as the interaction means that the wavefunctions of the pure states mix with the environment. If the state of the system is well known, the vector describing the state will end in a point close to the surface even if the state is mixed. In this case the relative phase of the system will also be known. Even if known at some point in time, the phase will not be known at any point in time, due to decoherence.

The decoherence process is caused by the fact that the superposition state will not evolve undisturbed, because its wavefunction is mixed with the surroundings. The system itself also has a finite relaxation time which will lead to decoherence as well. The loss of coherence is described in the Bloch sphere by letting the length of the vector decrease. This is further discussed in section 1.2.1.

If the lifetime of the excited state is denoted T_1, the coherence time T_2 is at most $2 \cdot T_1$. This happens when the coherence time is only limited by the spontaneous relaxation. Whenever there is decoherence due to interactions with the surroundings, the coherence time will be shorter. When nothing can be said about the phase any more, the vector describing the state will be parallel to the $w-$axis. [1].

The Rabi frequency Ω is a measurement of the interaction between the dipole moment $\boldsymbol{\mu} = -\langle g | e\boldsymbol{r} | e\rangle$ of a quantum system, in most cases an atom, and a time-varying electric field $\mathbf{E}$, e.g. from a laser field resonant with the transition of interest:

$$\Omega = \frac{\mathbf{E} \cdot \boldsymbol{\mu}}{\hbar} = 2\pi f \tag{1.4}$$

Here f is the non-angular Rabi frequency, which is often used when performing simulations and experiments.

Other quantities which are convenient to introduce when talking about optically driven transitions in two level quantum systems are the detuning, Δ, which is the difference between the frequency of the laser and the resonance frequency of the transition:

$$\Delta = \omega_r - \omega_L \tag{1.5}$$

and the generalized Rabi frequency which describes the rate at which the phase of the atomic state changes relative to the phase of the laser field:

$$\Omega_G = \sqrt{\Omega^2 + \Delta^2} \tag{1.6}$$

Now the Bloch vector can be described by the optical Bloch equations, where $\Omega = \Omega_R + i\Omega_I$ and ω_{eq} is the equilibrium state, usually $w = -1$:

$$\frac{\partial u}{\partial t} = -\Delta v - \frac{u}{T_2} + w\Omega_I \tag{1.7a}$$

$$\frac{\partial v}{\partial t} = \Delta u + w\Omega_R - \frac{v}{T_2} \tag{1.7b}$$

$$\frac{\partial w}{\partial t} = -v\Omega_R - \frac{w - w_{eq}}{T_1} - u\Omega_I \tag{1.7c}$$

These equations were used for simulations in the Bloch sphere, described in section 2. The complex part of the Rabi frequency corresponds to a part of the electromagnetic field not in phase with the two level system.

Yet another useful quantity for optically driven atomic transitions is the so called pulse area:

$$\theta = \Omega \cdot t \tag{1.8}$$

where t is the time during which the system is lased at, assuming a square pulse. When the laser frequency ω_L is completely resonant with the transition

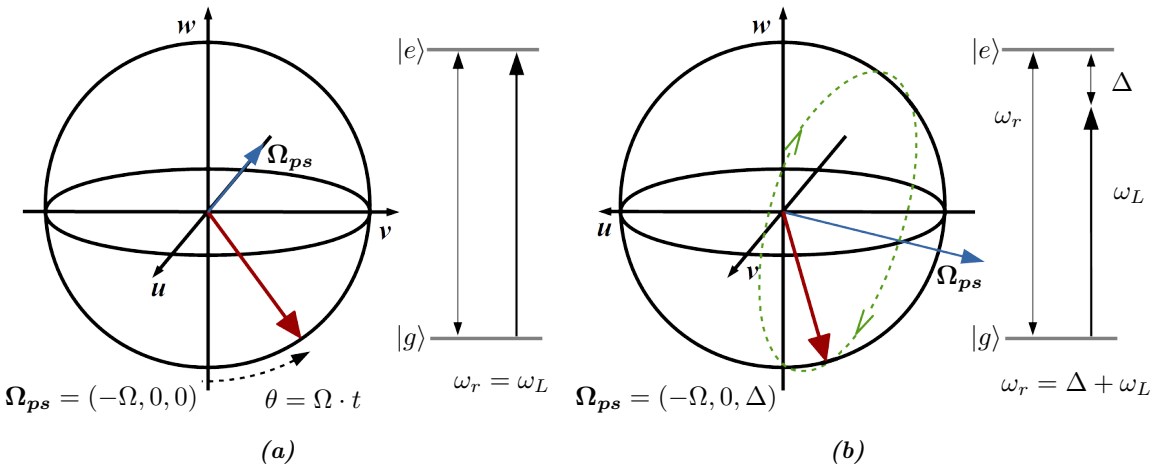

Figure 1.3: *(a) If the frequency of an applied laser field is in resonance with the transition in a two level system, the state vector will rotate around a pseudo vector* $\mathbf{\Omega_{ps}}$*, with* $|\mathbf{\Omega_{ps}}| = \Omega_G = \Omega$*, which lies in the* $-u$ *direction for a completely real Rabi frequency,* $\Omega = \Omega_R$*. If the Imaginary part* Ω_I *of the Rabi frequency is non-zero the pseudo vector will lie somewhere in the* $vu-$*plane.* ω_L *is the laser frequency, and* ω_r *is the resonance frequency. (b) If there is a difference* Δ *between the oscillation of the applied field and the resonance frequency of the system, the pseudo vector around which the state vector rotates will have an angle to the* $uv-$*plane. Now the detuning* Δ *is nonzero and thus* $\Omega_G \neq \Omega$*. Note the change in perspective of the coordinate system relative to (a).*

frequency ω_r, or in other words $\Delta = 0$, the pulse area describes the angle between the $w-$axis in the negative direction and the state vector.

For example, a $\pi-$pulse, $\theta = \pi$, corresponds to a transition from (0,0,-1) to (0,0,1), that is a transition from the ground state $|g\rangle$ to the excited state $|e\rangle$. Applying another π-pulse will rotate the state vector past the excited state back to the ground state $|g\rangle$. Thus the inversion w can be made to oscillate between 1 and -1, and the Bloch vector is said to rotate around a pseudo vector $\mathbf{\Omega_{ps}}$. This is described by $\mathbf{\Omega_{ps}} = (-\Omega_R, -\Omega_I, 0)$ for a complex Rabi frequency, where Ω is given by equation 1.4 and $|\mathbf{\Omega_{ps}}| = \Omega_G = \Omega$ as $\Delta = 0$, see equation 1.6. This situation is illustrated in figure 1.3a, assuming $\Omega = \Omega_R$.

If the laser frequency is slightly detuned from the resonance frequency, the inversion w will still oscillate between a maximum and a minimum value, but it will never reach complete inversion. The pseudo vector will no longer lie in the $uv-$plane, but slightly above or below, depending on whether the detuning results in a laser frequency ω_L higher or lower than the resonance frequency.

The pseudo vector will have the form $\mathbf{\Omega_{ps}} = (-\Omega_R, -\Omega_I, \Delta)$ with $|\mathbf{\Omega_{ps}}| = \Omega_G$. This is illustrated in figure 1.3b, still assuming $\Omega = \Omega_R$. Now a pulse area $\theta = \pi$ does not bring the system into the pure excited state but to a superposition state (w_{max}, u, v) where w_{max} is some maximum inversion for when the state vector has turned half a revolution around $\mathbf{\Omega_{ps}}$.

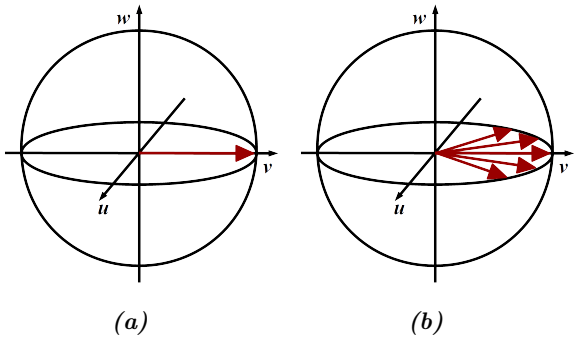

Figure 1.4: *(a) An ensemble of atoms with slightly different resonance frequencies are prepared in an initial superposition state. At time* t_0 *all atoms are coherent with the laser field. (b) After some time all the different atoms will have a different phase relative to the laser field, as they evolve slightly differently due to their different resonance frequencies.*

In figure 1.3b the trajectory of the tip of the state vector along the surface of the sphere is indicated by the dashed line. For a small detuning the state (w_{max}, u, v) will be close to the excited state.

1.2.1 Coherence

The importance of coherence has been noted previously, and will here be more rigorously explained with help of the Bloch sphere.

Imagine an atom oscillating between two states, driven by a laser with a frequency of $\omega_L = \omega_r - \Delta$. The phase of the atom is considered with the phase of the laser as reference. If this atom is left in a superposition state, for example (1,0,0), it will after some time no longer be in phase with the laser field as the laser frequency is detuned, thus it will be in a new state (u, v, 0). This can be illustrated by considering a detuned field with zero intensity: The pseudo vector will be $\boldsymbol{\Omega_{ps}} = (0, 0, \Delta)$, and the state vector would rotate around the $w-$axis at a speed proportional to Δ.

Figure 1.4 shows the idea of decoherence for an ensemble of atoms with similar but not equal resonance frequencies, illustrated through the Bloch picture. At time t_0 the whole ensemble is in phase with the laser field, but after some time the different states have evolved differently and the state vectors are spread out in the $uv-$plane. Taking an average of the vectors would result in a new vector parallel to the v-axis with a length shorter than 1.

1.3 Rare-Earth-Ion-Doped Crystals

As previously mentioned the rare-earth-elements are commonly used in the field of quantum information, often doped into inorganic crystals. These rare earth ion doped crystals are called RE-crystals. The rare-earth elements, also known as Lanthanides, are the elements which have an atomic number between 57 (lanthanum) and 70 (ytterbium). These occur as triply, positively charged ions when doped into some inorganic crystals commonly used in quantum information [1]. Optical transitions in the rare-earths involve electrons in the 4f-shell, which is only partially filled. The 4f-shell is shielded from the environment by the 5s- and 5p-shells.

RE-ions doped into inorganic crystals will individually have transition peaks with very narrow homogeneous line widths, which are important when doing accurate manipulations on the ions. However, as each ion experience a somewhat different crystalline field, they will be shifted with respect to each other and the narrow absorption peaks add up to a much broader spectrum. Due to the shielding of the 4f-shell they have long lifetimes for the hyperfine ground states and for the lowest excited states, and thus long coherence times at low temperatures. These properties are suitable for creating a qubit, as will be more thoroughly explained in the following.

1.3.1 Homogeneous Line Widths

The homogeneous linewidth of a transition peak is the frequency range within which a specific ion will absorb or emit radiation. The homogeneous broadening is due to dynamic processes of the ion and spontaneous relaxation between states. The dynamic contributions for an ion trapped in a crystal are very small, especially at cryogenic temperatures.

The homogeneous line width is limited by the spontaneous relaxation time, or life time, T_1 through the coherence time T_2. The coherence time can at most be twice the life time, $T_2 \leq 2T_1$. The correlation between the line width and the coherence time for a transition is described as

$$\Gamma_h = \frac{1}{\pi T_2} \tag{1.9}$$

Besides spontaneous relaxation, other processes contributing to decoherence in the dopant ions are disturbances in the surrounding crystal field due to spin flips in nearby atoms, together with the emission, absorption or scattering of phonons. By choosing a host crystal where the nuclear magnetic momenta are small or zero, disturbances from spin flips can be minimized. The flips can also be prevented by applying an external magnetic field. The phonons are avoided by keeping the sample at cryogenic temperatures of a few K, where phonons are negligible.

By compensating for these processes, transition peaks with narrow homogeneous line widths and long coherence times can be achieved. The narrow line widths suggest the use of narrow band laser pulses to only interact with a specific class of ions with transitions at specific frequencies, even if they are spatially very close to ions from other classes, absorbing at other frequencies. The long coherence times implies that the ions could be put in superposition states which could then evolve undisturbed for relatively long times without loosing coherence [1]. These are both important properties for quantum information processing.

1.3.2 Inhomogeneous Line Width

The inhomogeneous linewidth is due to interactions between the ions and between ions and the surroundings. The electric field from the crystal and nearby ions will for each individual ion be different, and this will cause the ionic levels to shift differently for each individual ion. The inhomogeneous linewidth is a result of energy shifts and homogeneous broadening of all ions summed together. This can be compared to the Doppler broadening for free atoms in a gas, where each individual atom has for itself a narrow absorption profile. The total width of the peak is however much broader, as the absorption profiles from many atoms with different Doppler shifts add together.

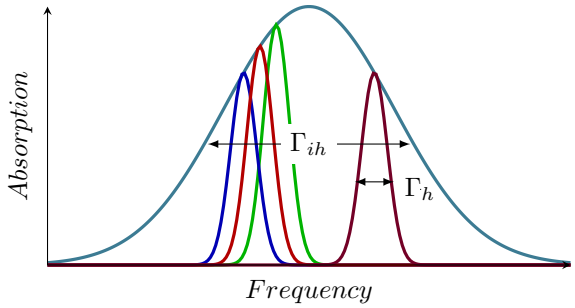

Figure 1.5: *Schematic picture of inhomogeneous broadening, Γ_{ih}. The transition peaks of all individual ions, each with the homogeneous broadening Γ_h, adds up to the total absorption spectrum which has a total width Γ_{ih}.*

The inhomogeneous broadening is typically a few GHz in weakly doped RE-crystals, but it can range from less than one to several hundred GHz. It does in general increase with increased dopant concentration [1, 4]. In figure 1.5 it is schematically shown how the spectral peaks of the individual ions add up to the total absorption profile of the crystal.

1.3.3 Hyperfine Levels

As mentioned above, levels with long coherence times are necessary for quantum computing. Such levels can be found in many RE-materials, for instance due to the hyperfine interaction, which is the interaction between the intrinsic spin I for the nucleus and the total angular momentum J for the electrons (also called IJ-splitting).

The hyperfine interaction causes the levels to split into doubly degenerate levels. In most cases, the dominating hyperfine interaction is a dipole interaction between the magnetic field of the nucleus and the magnetic field from the orbits. For the RE-ions trapped in a crystal, the orbital magnetic field is quenched by the crystal field, and therefore the hyperfine splitting in these ions is due to a second order hyperfine splitting caused by the quadropole electric moment in the nucleus and the electric field gradient from the electrons [1, 5].

The levels are conventionally labeled by the $z-$component of the nuclear spin, I_z, even though this often is not a good quantum number as the wavefunctions mix and can be far from the eigenstates. For Europium I=5/2, and thus the ground state levels are labeled $|\pm 1/2\rangle$, $|\pm 3/2\rangle$ and $|\pm 5/2\rangle$ with $\pm$ implying the degeneracy. This notation will henceforth be omitted, due to readability. The splitting is different for different isotopes, and the intrinsic spin can also be different. However, for ^{151}Eu and ^{153}Eu the nuclear spin is the same and the hyperfine levels are thus labeled in the same way. For the crystal trapped ions the hyperfine levels also vary for non-equivalent crystal sites.

As the splitting between the hyperfine levels is very small compared to the gross structure only given by the principal quantum number, the lifetime for an electron in a hyperfine ground level can be very long, up to several days [1]. They can therefore be used for semi-permanent memory storage. The life times of the excited states are not as long as for the ground state, but they can still be long enough to use for high-speed processing.

Transfers between hyperfine levels can be made either via an excited state using optical pulses, or directly using radio frequency pulses. At energies corresponding to typical hyperfine splittings the phonon density of states will be low, and at cryogenic temperatures the relaxation of the electrons will thus be slow.

1.3.4 Oscillator Strengths

As is known from atomic physics, only certain transitions within an atom are allowed. Whether a transition is allowed or not depends on the quantum numbers n, s, l and m_l, or in other words on the overlap of the wave functions. When quantum systems are brought together their wavefunctions mix, and the quantum numbers derived for describing the pure eigenstates might no longer be good quantum numbers for describing the mixed states. The mixing allows for transitions that might not be allowed if the eigenstate wavefunctions were not mixed, and thus some transitions that should not be possible can be observed. In an atom the electronic wavefunctions mix, and for heavy nuclei the conventionally used LS-coupling is often insufficient for a satisfactory description of the system.

The transition strength, or oscillator strength, for a transition is proportional to the probability of the transition. High oscillator strength means that the transition has high probability to happen, which means that the power needed to drive it optically is not so high and that the relaxation is fast. Therefore weakly allowed transitions are chosen for optical information processing with very small oscillator strengths compared to the allowed dipole transitions.

The oscillator strength is proportional to the square of the dipole moment, and thus the Rabi frequency is proportional to the square root of the oscillator strength (see equation 1.4).

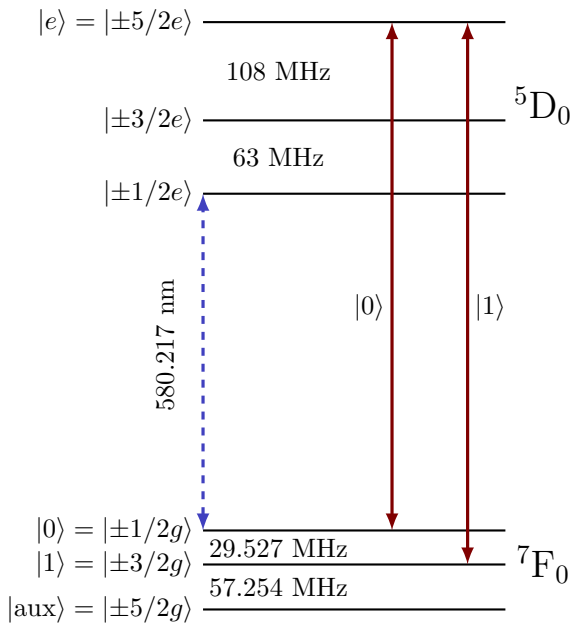

Figure 1.6: *Electronic structure for the Eu-ions in $^{151}Eu^{3+}$:Y_2SiO_5 for the two levels of interest [6, 7]. The red arrows indicate the transitions used for the NOT-gate described in section 1.1.1.*

1.3.5 The Europium Doped Yttrium Orthosilicate Crystal

In this experiment a Y_2SiO_5 crystal doped with 0.1% $^{151}Eu^{3+}$ was used. Experiments have been done with a very similar crystal $^{153}Eu^{3+}$:Y_2SiO_5, and therefore much could be learned about the properties of the Eu^{3+}-ion [7, 6].

Europium has atomic number 63, and thus the Eu^{3+}-ion has 60 electrons, of which 6 are in the 4f-shell [5]. The ground level is the $^7F_0$-level and the excited level used in this project was the $^5D_0$ level. Each of these two levels are split into three hyperfine levels, with the structure shown in figure 1.6. Both levels have a total angular momentum J=0, which means they do not possess any first order electronic magnetic moment. They are therefore not sensitive to spin flips in the crystal which causes decoherence, as mentioned previously [4]. This means the spontaneous relaxation is slow, and thus the coherence times at cryogenic temperatures will be long as desired [6].

The Y_2SiO_5 crystal is a good host material due to the small magnetic moments of its constituent atoms, which further reduces decoherence in the Eu ions caused by spin flips in the crystal. Due to the minimized interactions between the ions and the host material, the homogeneous linewidths in $^{153}Eu^{3+}$:Y_2SiO_5 is the narrowest linewidth measured for any solid, measured to 122 respectively 167 Hz at 1.4 K for two different crystal sites [8].

When the Y_2SiO_5 crystal is doped the $^{151}Eu^{3+}$ ions substitute for Y^{3+} in two inequivalent crystal sites. In this work ions at site 2 were used, corresponding to the wider line width for $^{153}Eu^{3+}$. The reason for why the ions at site 2, and also why isotope 151 were used is due to limitations in the experimental equipment. The hyperfine splittings are smallest for isotope 151 at site 2, and the equipment could not handle bigger energy splittings. This is further discussed in section 3.2.

The inhomogeneous broadening in $^{151}Eu^{3+}$:Y_2SiO_5 with 0.1% dopant concentration at site 2 is 1.4 GHz [4], and it increases with dopant concentration. Thus the narrow transitions peaks of the individual ions are not accessible in the actual absorption spectrum. This can be accounted for using the method of hole burning, which is further discussed in section 1.4.

The crystal has three directions which have different absorption properties. These directions are labeled b, D_1 and D_2. The absorption properties are also different for the two sites. For site 2 the b-direction has the highest absorption coefficient [4]. The laser beam was sent along the D_2-axis with the electric field parallel to the $b-$axis to maximize the absorption, and thus the transfer efficiency.

The dimensions of the crystal were 5.5×5.5×8.6 mm, with the crystalline D_2-axis in the $z-$direction. Thus the effective thickness of the crystal was 8.6 mm, which is rather thick. This has the advantage that the signal-to-noise ratio should be high, and the disadvantage that the beam can not be focused too hard, as the focus should be approximately homogeneous throughout the crystal. This is also discussed in section 5.2.

In section 1.1.1 the implementation of the NOT-gate in the europium ion was described. In figure 1.6 the ground states $|1/2g\rangle$ and $|3/2g\rangle$ corresponds to the states $|0\rangle$ and $|1\rangle$ in figure 1.1 respectively. The ground state $|5/2g\rangle$ corresponds to the $|\text{aux}\rangle$ and the excited state $|e\rangle$ is $|5/2e\rangle$.

1.4 Hole Burning

Hole burning is a method for investigating, but also manipulating, the properties of an absorption spectrum. In the inhomogeneously broadened spectrum given by the ions in the RE-crystal one frequency will correspond to different transitions for different ions due to the shifted energy levels, and all ions that actually have a desired transition at the specific frequency might not be in the correct hyperfine state to absorb at this frequency. Thus some manipulation is

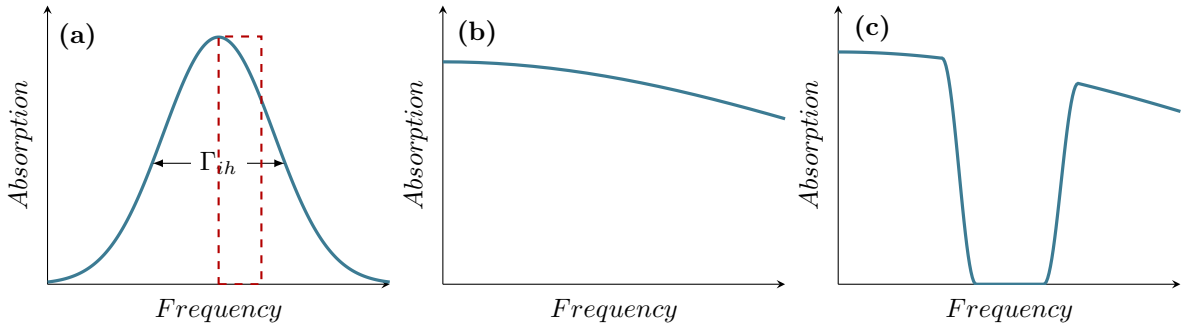

Figure 1.7: *Here is shown the idea of the spectral pit. Figure (a) shows the entire homogeneously broadened peak. Figure (b) shows the part of the peak inside the red, dashed box in figure (a). In figure (c) a spectral pit has been burned in this region of the spectrum.*

needed before the crystal could be used for any logical operations.

Hole burning refers to the creation of a spectral hole in an absorption spectrum by burning at a specific frequency with a laser. The ions absorbing at this frequency will then be excited, and the absorption will decrease as the absorbing ions are excited. These spectral holes are usually not very long lived as the ions will soon deexcite. However, the Eu-ions have three different ground levels, and when the ions are excited from one ground level they could deexcite into another. Thus semi-permament sprectral holes can be created in these ions, and also in other, similar ions.

To deplete a minor region of the spectrum, instead of just a narrow hole, the burning can be done by sweeping across a frequency interval instead of just burning at a single frequency. Then the region of low absorption is called a spectral pit. The inhomogeneous broadening of the ions in the crystal is schematically illustrated in 1.7a. Figure 1.7b zooms in on a specific area marked with a red, dashed box in 1.7a. Figure 1.7c shows the same zoomed in area but now a spectral pit has been created.

The spectral hole, or pit, is limited by the possible transitions for the element in question. The pit can only be so wide that the excited ions can relax to a state outside the pit, otherwise the pit can not be emptied. To create the desired narrow absorption peak to use for quantum processing, some ions absorbing within a very narrow frequency interval are burnt back into the pit.

Figure 1.8a shows two spectral pits corresponding to the two transitions indicated by red arrows in figure 1.6 and 1.1. In each pit an absorption peak can be created, corresponding to the transition from one of the hyperfine ground levels to one of the excited levels. The distance between the peaks is exactly the

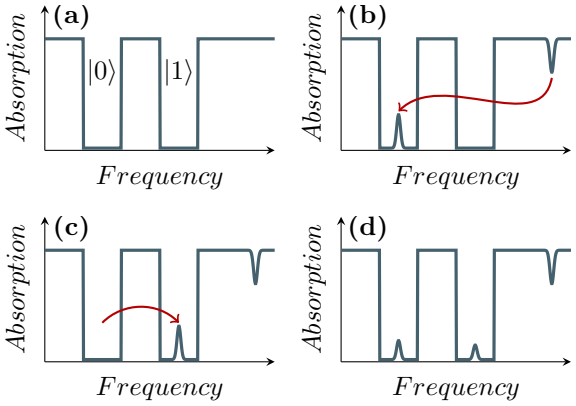

Figure 1.8: *Schematic view of how the qubit is constructed. In (a) two spectral pits have been burned corresponding to transitions between two different ground states, $|0\rangle$ and $|1\rangle$, to an excited state. In (b) atoms with the desired transitions are burnt back into the $|0\rangle -$state from a third auxiliary state $|aux\rangle$. (c) The ions can then be moved from $|0\rangle$ to $|1\rangle$ via the excited state using optical pulses. (d) If the transition is not done completely, there will at readout be a spectral peak in each of the two pits. The area under the peaks will depend on the precise operation.*

spectral distance between the two ground levels, and the ions can be optically transferred from one pit, $|0\rangle$, to the other pit, $|1\rangle$, via the excited state, $|e\rangle$. As has been mentioned previously the two ground states $|1/2g\rangle$ and $|3/2g\rangle$ has been used for the states $|0\rangle$ and $|1\rangle$ respectively. The excited state $|5/2e\rangle$ in the $^5D_0$ level has been used as $|e\rangle$. These levels and the associated transitions are indicated in figure 1.6.

As the two spectral pits are created, all ions with the correct transitions within the pits will be transferred into the third state, $|5/2g\rangle$. This state has previously been referred to as the auxiliary state $|\text{aux}\rangle$, and is also indicated in figure 1.6. The qubit is cre-

ated by moving some ions which have the desired transitions back into one of the pits, as in figure 1.8b. Any ion with the correct frequencies inside the pits, but not within the desired narrow peak, should however be left in the auxiliary state.

Once the qubit has been created, ions can be transferred between the ground states $|0\rangle$ and $|1\rangle$ via $|e\rangle$ using laser pulses (see figure 1.8c). If all atoms are not completely transferred the readout spectrum will show a peak in both pits, as the wavefunctions for the atoms will collapse to one of the states before or at readout, see figure 1.8d. These peaks will be smaller than the peak in 1.8c and at most they will together have the same area as the peak in 1.8c, assuming the two transitions have the same transition strength. As the absorption is proportional to the strength of the transition, the absorption peak will be bigger for a stronger transitions. If there is any population left in the excited state $|e\rangle$ at readout the total area of the absorption peaks will be smaller, as the readout pulse will cause stimulated emission.

2 Simulations

The purpose of this project was to create a prototype qubit, and to achieve as high fidelity as possible for transitions between the two qubit states. How the qubit is created was explained in section 1. In section 1.4 it was explained how all ions absorbing at the wrong frequencies were removed from a part of the absorption spectrum, and a schematic figure of how the spectrum of the qubit looks can be seen in figure 1.8b-d.

Although the peaks inside the spectral pits are narrow, they are still broader than the homogeneous line width of the individual ions, and the difference in resonance frequency for the different ions will cause them to respond differently to a laser pulse of a specific frequency. Thus a regular square pulse could not be used for making the transfers, but instead a complex hyperbolic sechant pulse, also called sech or sechyp pulse, was used to make the transfers.

The sechyp pulse is designed to accurately transfer an ensamble of ions with slightly different resonance frequencies between two atomic states. It does this by doing a frequency sweep in time over the peak that is to be transferred. The Bloch vector will move from the ground to the excited state in a spiral shape, and the transfer efficiency is well over what could be obtained for a frequency sweep with either square or Gaussian pulses [9].

As the sechyp pulse does a frequency sweep in time, the Rabi frequency will be time dependent. This time dependence is given by:

$$\Omega(t) = \Omega_0 \left[\mathrm{sech}(\beta(t - t_0))\right]^{1+i\mu} \tag{2.1}$$

where Ω_0 is the maximum Rabi frequency, μ is a real constant given by the magnitude of the frequency modulation and β depends on the time duration of the pulse [1]. From this follow also the relations

$$|\Omega(t)| = \Omega_0 \mathrm{sech}(\beta(t - t_0)) \tag{2.2a}$$
$$\Delta\nu(t) = \mu\beta \tanh(\beta(t - t_0)) \tag{2.2b}$$

where $\Delta\nu$ is the deviation from the center frequency of the laser.

The full width half maximum, FWHM, of the amplitude of the pulse is then given as $2.6/\beta$, and when μ is non zero the frequency of the laser changes with time. When $\mu \geq 2$ and $\Omega_0 \geq \mu\beta$ the inversion becomes insensitive to the maximum Rabi frequency, and thus insensitive to intensity fluctuation in the laser beam. The sechyp pulse is also highly frequency selective, with a sharper selection for increased μ and decreased β [1].

The properties of the sechyp pulse is shown in figure 2.1. In the top plot the population transfer with respect to resonance frequency is shown. The 0-frequency denotes the central laser frequency. In the two plots at the bottom the time depending Rabi frequency and the frequency sweep of the sechyp pulse can be seen, which are the two relations given in equation 2.2.

The population transfer is very efficient within a frequency range around the center laser frequency for the pulse shown in figure 2.1. However, the transfer efficiency is still sensitive to very small changes in the pulses, and therefore simulations were made to design pulses which should optimize the transfer efficiency prior to the experimental measurements. The program used for this was based on the Bloch equations, equation 1.7a-c. The output showed the final state of the Bloch vector depending on the resonance frequency of the ion, along with the transfer efficiency and the properties of the transfer pulse.

The program initially showed the final state for the Bloch vector and the transfer efficiency for a sechyp pulse given the length and time FWHM of the pulse, the maximum non-angular Rabi Frequency and a frequency width of the sechyp pulse. Figure 2.1 shows the output from this program for a pulse with frequency $f = 0.51$ MHz, FWHM of 0.96 MHz, a total time duration of 5.11 μs and a time FWHM of 1.71

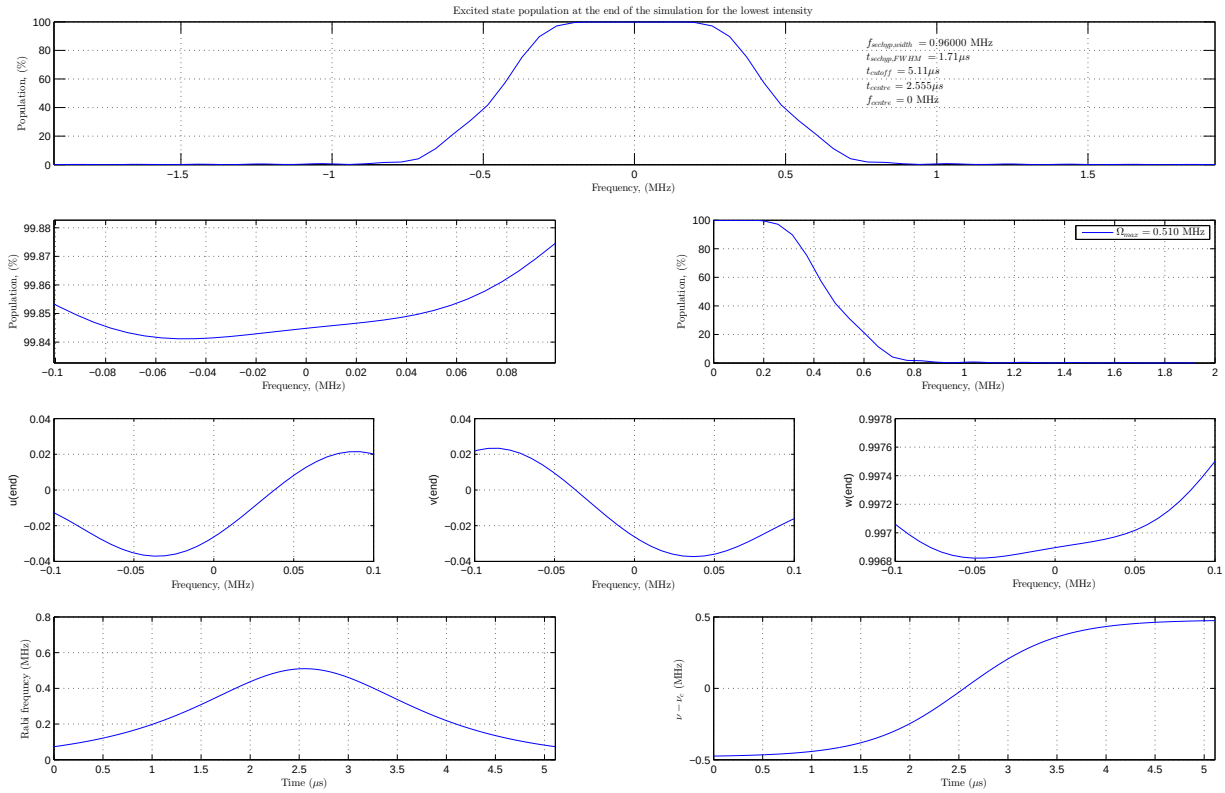

Figure 2.1: *Simulation for transfer efficiency for a sechyp pulse with non-angular Rabi frequency* $f = 0.51$ *MHz, FWHM of* 0.96 *MHz, a total time duration of 5.11* μ*s and a time FWHM of 1.71* μ*s. The topmost plot shows the population inversion over a frequency interval inside the pit. As is seen only a small interval around the center laser frequency is effected by the pulse. The left plot in the second row shows the center of the topmost plot and the right plot in the second row shows the right half of the topmost plot. The third row shows the* u*,* v *and* w *components of the Bloch vector depending on frequency. As desired it is close to (0,0,1), which means this pulse should give a high transfer efficiency. The last two plots show the Rabi frequency and the frequency of the pulse versus time respectively.*

μs. This is the same pulse as in figure 2.2 and 2.3, and the pulse denoted "pulse 1" in section 4.4.

The simulations were done for the transitions $|1/2g\rangle \rightarrow |5/2e\rangle$ and $|3/2g\rangle \rightarrow |5/2e\rangle$ in figure 1.6, which corresponds to $|0\rangle \rightarrow |e\rangle$ and $|1\rangle \rightarrow |e\rangle$ respectively in section 1. A pulse was optimized to each of these transitions considering to the maximum Rabi frequency the setup could produce for either transition (see section 4.3). Thus the maximum Rabi frequency needed to be measured before the pulses could be fully designed.

As can be seen the simulated pulse should give a transfer efficiency of more than 99.8 %. This does however only consider the spatial center of the beam where the intensity is highest, but says nothing about what would happen when the intensity decreased towards the edges of the beam.

Equation 1.4 shows the relationship between the Rabi frequency and the electric field $\mathbf{E}$, and 1.8 shows the relation between the angular Rabi frequency Ω and the pulse area θ assuming a square pulse. Equation 1.8 is not valid for the sechyp pulse, but the proportionality is still valid. Thus the Rabi frequency, and therefore also the pulse area and the transfer efficiency, decreases towards the edges of the beam.

Assuming the electric field has a Gaussian shape a spatial coordinate was also implemented into the program. The result from these simulations assuming a focus of 100 μm is shown in figures 2.2 and 2.3.

In figure 2.2 the u and v are close to zero and w close to 1 for ions close to the beam center. This means that they are close to the $|e\rangle$ −state with

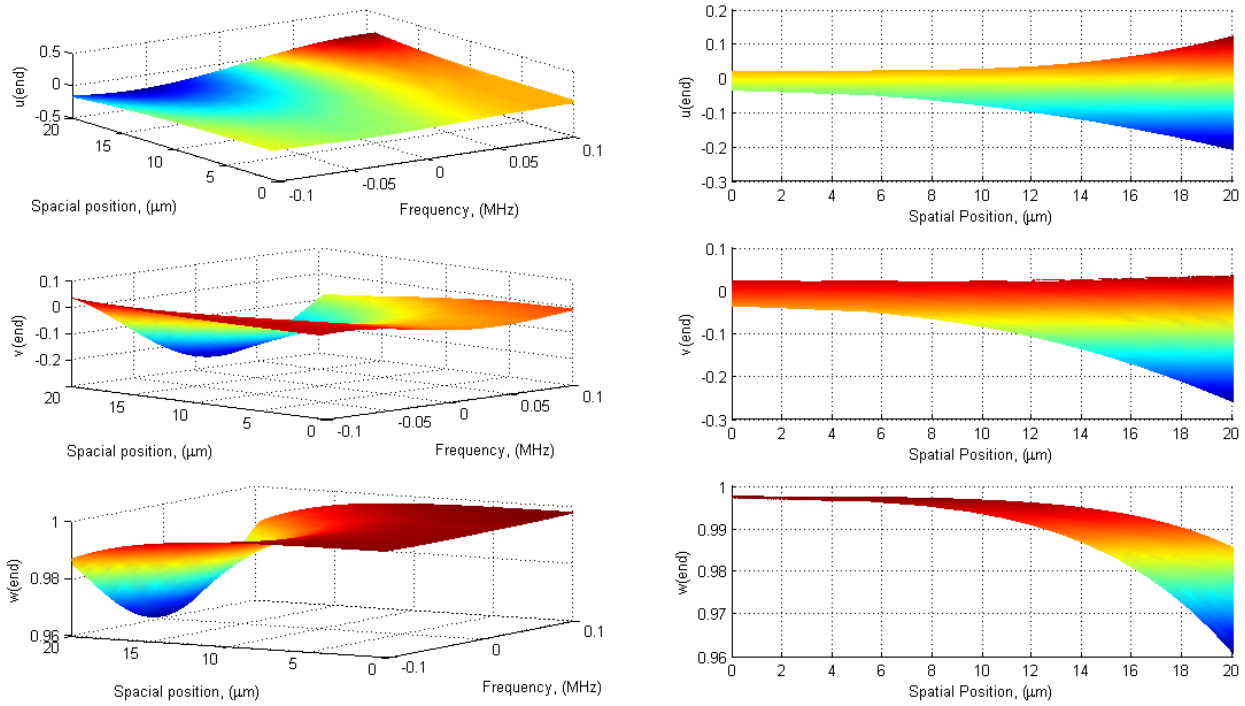

Figure 2.2: *Simulation for transfer efficiency for a sechyp pulse with non-angular Rabi frequency* $f = 0.51$ *MHz, FWHM of* 0.96 *MHz, a total time duration of 5.11* μ*s and a time FWHM of 1.71* μ*s, which is the same as in figure 2.1. The left column shows the* u, v *and* w *components over the spectral interval of the transition peak, and the right column shows the same plot from a perspective that clearly shows the spatial dependence from the beam center.*

$(u, v, w) = (0,0,1)$, which is the pure excited state. Around 15 μm from the center of the beam the $u-$ and $v-$components start to deviate notably from 0 and the $w-$component starts to decrease. Thus only the light which comes from the center of the beam was desired for measurements.

3 Setup

To create the simulated pulses in reality, great care had to be taken in setting up the experiment. The laser needed to be very stable, and very accurate adjustments of the laser frequency had to be possible. The basic setup is shown in figure 3.1.

A dye laser was used to create a finely tunable beam. The beam was coupled to a Pound-Drever-Hall locking system to achieve a stable frequency with a narrow bandwidth [10]. A single mode fiber was used to assure that the beam spatially had a Gaussian shape, and to allow for creating the sechyp pulses the light was let to double pass through an acousto-optic modulator (AOM) which allowed for fast and precise frequency modulations. The crystal sample was kept in a cryostat to allow for low enough temperatures to make the homogeneous absorption peaks narrow by making phonon interactions negligible.

A pinhole was used to only select information from the center of the beam where the intensity, and thus the amplitude of the electric field and the transfer efficiency, was the highest. How much of the beam that was selected was based of the simulation described in section 2, and how the pinhole was set up is described in section 3.4.

3.1 The Dye Laser

To be able to create the desired pulses a tunable laser, stable in both intensity and frequency, was needed. To aquire this a dye laser was used. The dye laser works by modulating the beam of a pump laser by letting the beam hit a jet of liquid dye.

The frequency of the pump laser is fixed and must be higher than the desired frequency of the dye laser. Depending on the dye different frequency intervals can be reached. The dye is dissolved in a solvent

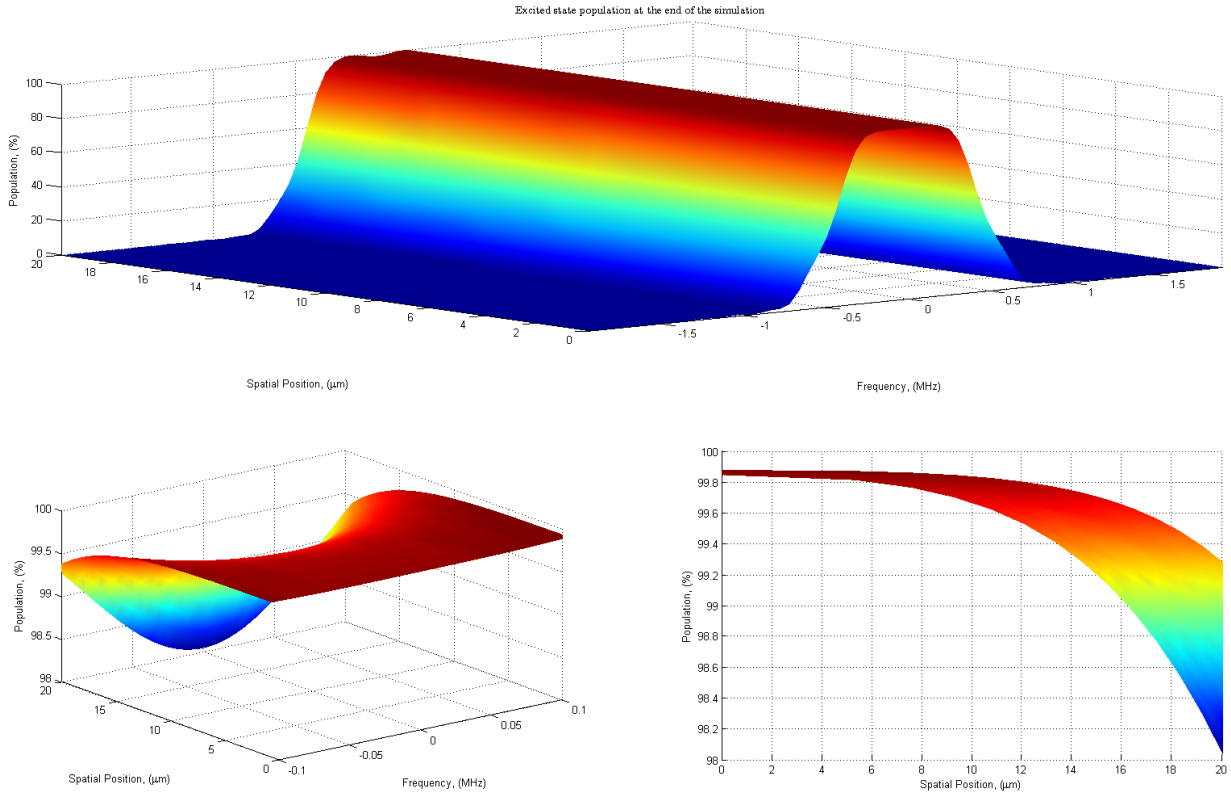

Figure 2.3: *Simulation for transfer efficiency for a sechyp pulse with non-angular Rabi frequency* $f = 0.51$ *MHz, FWHM of* 0.96 *MHz, a total time duration of 5.11* μs *and a time FWHM of 1.71* μs*, which is the same as in figure 2.1 and 2.2. The top plot shows the fraction of the total population which has been transferred to the excited state depending on frequency and distance from the beam center. The two lower plots show the center of the first plot from* $f = -0.1$ *to* 0.1 *MHz. In the lower right plot the spatial dependence in clear.*

which is circulated in a closed system. A very smooth jet is created where the laser beam from the pump laser intersects with the dye. The atoms in the dye are excited by the pump laser beam and when relaxing they emit within a wide frequency interval.

The dye laser had a cavity which allowed for precise adjustments to allow for selection of the desired wavelength of 580.217 nm, which is the resonance frequency of the $^7F_0 \rightarrow ^5D_0$ transition, as shown in figure 1.6. The pump laser gave out a beam of 6 W and the output after the dye laser was 1 W.

The laser cavity was coupled to a Pound-Drever-Hall locking system. This consisted of a cavity with resonances equally spaced in frequency space, and the laser could be locked to one of these frequency modes. Light was reflected inside the cavity and detected outside to create an error signal for adjusting the dye laser [10, 11]. This resulted in a laser band width of about 10 Hz.

3.2 Acusto-Optic Modulators

To allow for the frequency sweeps and intensity variations in the sechyp pulses an AOM was used. An AOM alters the frequency of the light by sending a sound wave through a crystal. The refractive index of the crystal is periodically modified by the sound wave to create an acoustic grating. The beam passed through the AOM twice as the light gets deflected when passing through, by an angle θ according to

$$\theta = \frac{\lambda F}{v} = \frac{\lambda}{\Lambda} \tag{3.1}$$

where λ is the optic wavelength in the crystal, F is the frequency and v is the speed of the acoustic wave and Λ is the acoustic wavelength. As is seen the deflection angle varies depending on the modulation frequency.

This was compensated for by letting the light pass twice, once in each direction. Thus it was deflected an equal amount each time but in different directions, and the net deflection became zero as is shown in figure 3.1.

The light passing through the AOM picks up the properties of the sound wave to get a new frequency $\nu_{diff} = \nu_{laser} + F \cdot m$, where m is the order of diffraction. The AOM is most efficient for $m = 1$ and and thus the intensity will be highest for $m = 1$. However, some light will always slip through without being modulated and therefore some intensity will be lost each time the beam passes through an AOM. The intensity of the deflected beam, I, is related to the incoming beam intensity, I_0, as

$$\frac{I}{I_0} = \xi sin^2\left(\frac{\pi}{2}\sqrt{\frac{P}{P_0}}\right) \tag{3.2}$$

where P is the radio frequency power to the AOM and P_0 is the optimal power given by the properties of the specific AOM, at which the efficiency is highest. ξ is the maximum efficiency of the AOM, typically between 60-95%. For the AOM used in the experiment, $\xi = 84\%$. However, ξ also depends on the frequency, as the AOM is not equally efficient for all frequencies.

The efficiency is highest for some center frequency specific for each modulator. Typical frequency modulations for an AOM lies between 50 and 500 MHz. The AOM input, and thus the diffraction of the the light, can often be tuned within $\pm 25\%$ of the AOM center frequency. By using several modulators after each other, or by letting the light pass twice through one modulator, a frequency modulation of several hundred MHz can be achieved [1].

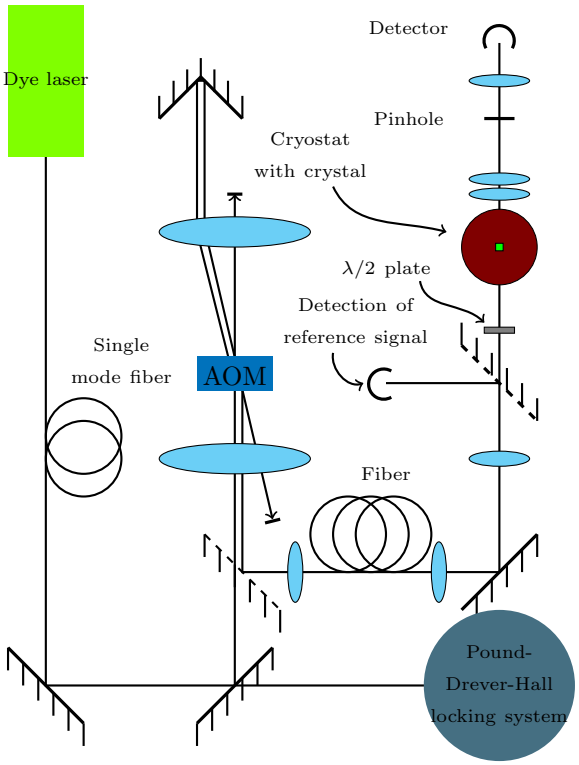

Figure 3.1: *Schematic over essential parts of the setup. A dye laser was used to finely modulate the beam of a pump laser to the desired frequency of 580.217 nm . A Pound-Drever-Hall locking cavity was used to assure a stable frequency with narrow band width. To assure that the focus spatially had a Gaussian shape the beam was sent through a single mode fiber, and an acusto-optic modulator (AOM) was used to allow for frequency sweeps and intensity modulations of the beam. Carefully selected lenses were used to create the desired size and position of the focus and a pinhole was used to only select light from the center of the beam for detection. To align the electric field with the b direction of the crystal a $\lambda/2$ plate was placed just before the cryostat.*

3.3 The Cryostat

The sample was cooled using a cryostat, which consisted of three vacuum shields with liquid nitrogen and helium in between. In the center was a chamber in which the sample was placed. This chamber could be filled with liquid helium and was surrounded by a vacuum shield. Between the innermost and the middle vacuum shield was liquid helium, and between the middle and outermost vacuum shields was liquid nitrogen. Small windows allowed for a view of the sample inside the chamber from four different directions.

When the sample was to be cooled liquid helium was let into the sample chamber to cover and cool the sample. To minimize the disturbances from scattering of phonons in the ions the crystal was cooled to 2.17 K at a pressure of 40 mBar. At these conditions helium is super fluid, which means that it has infinite heat conductivity and thus there will be no disturbances from gas bubbles in the liquid due to uneven temperatures in the sample chamber.

3.4 Placing The Pinhole

Figure 2.3 shows the population in the excited state versus spatial and spectral position. Here it can be seen that the population starts to decrease notably about 15 μm from the beam center. Thus only the light from the center of the beam is desired, which was achieved using a pinhole. The setup of the pinhole is shown in figure 3.1. After the cryostat the light was

collimated with a 25 cm lens. It was then focused on a 50 μm pinhole with a 40 cm lens. A small script for calculating how much of the beam would pass through the pinhole was written for a specific setup, the setup described above would let through a part of the beam with a radius of $\sim 16\mu$m. As is seen in figure 2.3 the transfer efficiency for the light that passes through should never go beneath 99%.

4 Results

As mentioned previously the goal of this project was to create a prototype qubit. In order to be able to make operations with the qubit, transfers between the two qubit states $|0\rangle$ and $|1\rangle$ must be possible to do with very high fidelity. According to the simulations presented in section 2 a population transfer of more than 99% should be achievable for a single transfer between the two states $|0\rangle \leftrightarrow |e\rangle$, which is the transition $|1/2g\rangle \leftrightarrow |5/2e\rangle$ for the actual ion.

However, the transfer $|e\rangle \rightarrow |1\rangle$ was also needed to make a complete transfer between the two qubit states. In section 4.4 it is explained how the transfer efficiency was measured and evaluated and the results from this is presented. Before these measurements were done some other properties of the sample was studied: the oscillator strengths and the possible Rabi frequencies.

Prior to any actual measurements, it was verified that only the wanted class of ions with the correct frequencies was moved back into the spectral pits. This was to assure that the system behaved as expected. This was done for all nine transitions, and all but one peak was shown to contain only ions of the wanted ion class. This peak did not correspond to one of the qubit transitions and was thus not a problem. How this verification was done is explained in section 4.1.

In figure 1.6 it can be seen that between the two levels of interest there are nine possible transfers in total. Pulses for the two transitions of interest, $|1/2g\rangle \leftrightarrow |5/2e\rangle$ and $|3/2g\rangle \leftrightarrow |5/2e\rangle$, had to be optimized using the program described in section 2. As mentioned previously a high Rabi frequency is desired for making high efficiency transfers, as the pulse times can then be kept short. Therefore is was investigated what Rabi frequencies could be achieved with the current setup for the two transitions. This was done by combining the results from two different measurements.

One method used for measuring the Rabi frequencies of the transitions was to measure the relative oscillator strengths. In section 4.2 it is described how this mas done for the nine possible transitions. As mentioned in section 1.3.4 the Rabi frequency is proportional to the square root of the oscillator strength. However, as the measurement didn't give the proportionality constant, some additional measurement was required to obtain the absolute Rabi frequencies that could be obtained.

The absolute Rabi frequency were thus also measured for seven of the nine possible transitions. These measurements gave the maximum Rabi frequency that could be obtained for each of the seven measured transitions with the used setup. This is presented in section 4.3. The reason to why these measurement was not done for two of the transitions was because one of them was too weak, and the other contained ions that were not within the desired ion class, which is further explained is section 4.1.

4.1 Verifying The Ion-class

To only move the desired ions back into the spectral pits is not trivial. Therefore it was verified that only the desired ions were burnt back before any measurements were taken. To do so the crystal was prepared by creating three pits corresponding to the transitions from one of the hyperfine ground states to each of the three excited states at a time. Ions were then burnt back into the ground state, which would yield a peak in each of the three pits. By burning at one of the peaks all three should disappear, as the ions should be moved to a different ground state through this procedure.

For the $|1/2g\rangle$ and $|3/2g\rangle$ state to all three excited states all three peaks were there, though only two were visible in the former case. For the $|5/2g\rangle$ state there was however something else in the peak $|5/2g\rangle \rightarrow |5/2e\rangle$.

Figure 4.1 shows some of the obtained absorption spectra. The absorption is given in αL where α is the absorption coefficient and L is the optical length of the absorbing medium. The plots show the readout of 2 MHz around each peak, ignoring the spectral distance between the peaks. This could be corrected for using the values given in figure 1.6. This was not done due to clarity, as the region of interest is very small compared to the total spectral interval of the different transitions.

In figure 4.1a the peaks from the $|3/2g\rangle$ state to all three excited states can be seen. Burning at one of the peaks caused all peaks to disappear, as was expected. The same can be seen for the $|1/2g\rangle$ state in figure 4.1b, though in the right spectrum there is also a peak corresponding to the transition $|5/2g\rangle \rightarrow |1/2e\rangle$ at 4 MHz. When the ions are burnt away from the $|1/2g\rangle$ state they will end up in either $|3/2g\rangle$ or $|5/2g\rangle$, which is the explanation to this new peak.

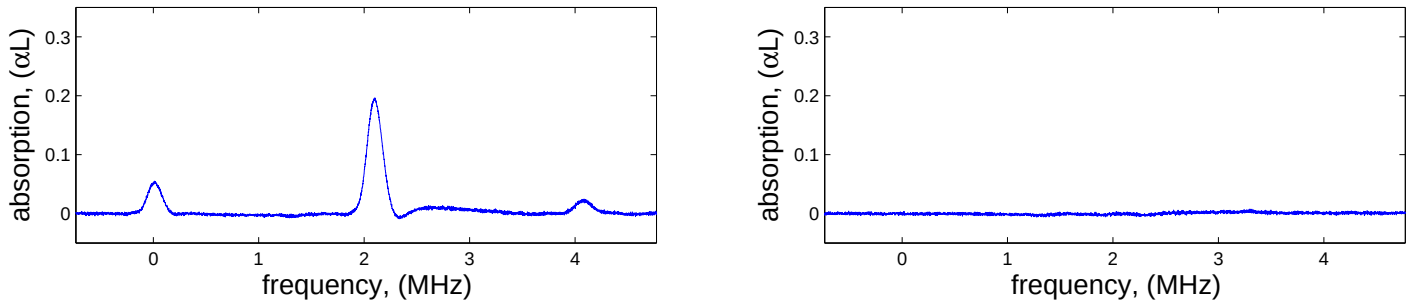

(a) *Readout spectra of the transitions from $|3/2g\rangle$ to all three excited states. (left) Scan over an interval of 2 MHz centered on each transitions peak. From left to right the peaks correspond to the transitions $|3/2g\rangle \rightarrow |1/2e\rangle$, $|3/2g\rangle \rightarrow |3/2e\rangle$ and $|3/2g\rangle \rightarrow |5/2e\rangle$. (right) burning at the transition $|3/2g\rangle \rightarrow |1/2e\rangle$ causes all three peaks to disappear, as the ions are moved into a different ground state and do not absorb at the original frequencies any more. Burning at $|3/2g\rangle \rightarrow |3/2e\rangle$ and $|3/2g\rangle \rightarrow |5/2e\rangle$ produces the same result.*

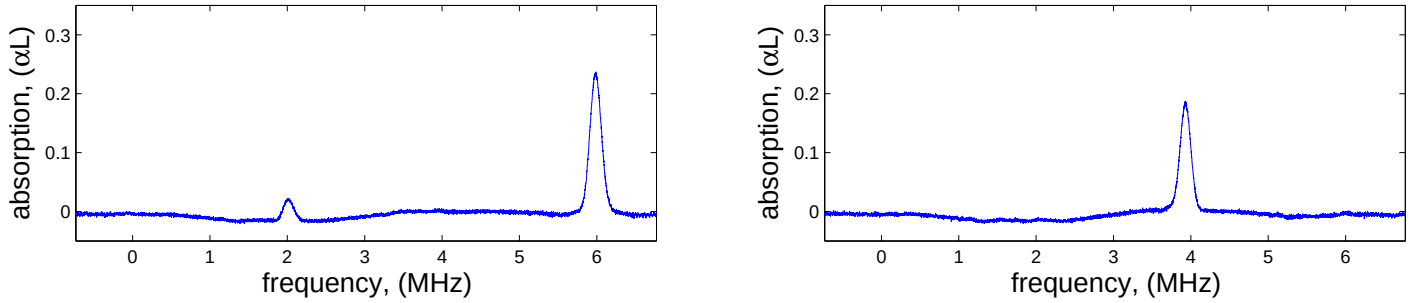

(b) *Readout spectra of the transitions from $|1/2g\rangle$ to all three excited states and at 4 MHz the transition $|5/2g\rangle \rightarrow |1/2e\rangle$. (left) The transitions $|1/2g\rangle \rightarrow |3/2e\rangle$ and $|1/2g\rangle \rightarrow |5/2e\rangle$ are visible at 2 and 6 MHz respectively. No peak corresponding to $|1/2g\rangle \rightarrow |1/2e\rangle$ at 0 MHz is visible, nor at $|5/2g\rangle \rightarrow |1/2e\rangle$ at 4 MHz, where there should not be one as all ions should be in the $|1/2g\rangle$ state. (right) after burning at the transition $|1/2g\rangle \rightarrow |1/2e\rangle$ at 0 MHz where no peak was visible, the two visible peaks have disappeared and a peak has been created at $|5/2g\rangle \rightarrow |1/2e\rangle$, as ions have been moved to the $|5/2g\rangle$ and $|3/2g\rangle$ states from the $|1/2g\rangle$ state. The lack of a visible peak at 0 MHz means that the transition $|1/2g\rangle \rightarrow |1/2e\rangle$ is very weak.*

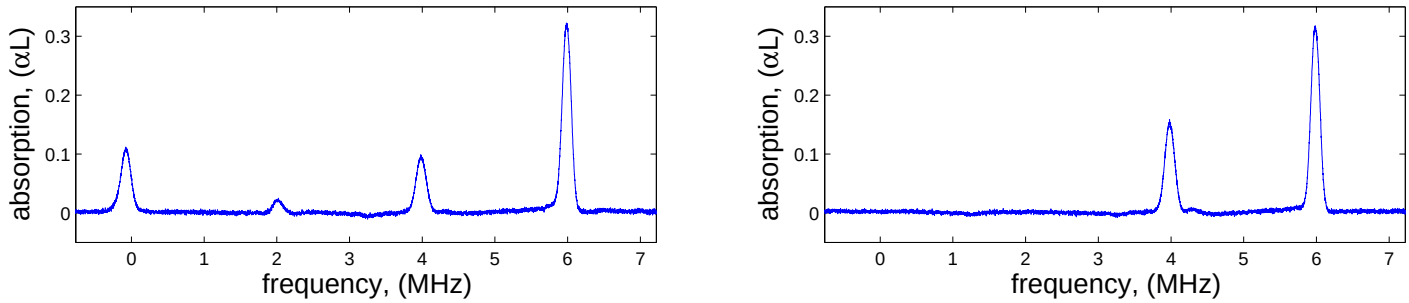

(c) *Readout spectra of the transitions from $|5/2g\rangle$ to all three excited states and the transition $|1/2g\rangle \rightarrow |5/2e\rangle$ at 4 MHz. (left) The three peaks corresponding to the transitions $|5/2g\rangle \rightarrow |1/2e\rangle$, $|5/2g\rangle \rightarrow |3/2e\rangle$ and $|5/2g\rangle \rightarrow |5/2e\rangle$, positioned at 0, 2 and 6 MHz respectively, are present as expected. However, there is also a peak at 4 MHz. This comes from some unwanted ion class, and must therefore be some other transition than $|1/2g\rangle \rightarrow |5/2e\rangle$. (right) After burning at $|5/2g\rangle \rightarrow |1/2e\rangle$ the two first peaks disappear. The last one, corresponding to $|5/2g\rangle \rightarrow |5/2e\rangle$ is still there, although somewhat smaller. This means that also in this peak there are unwanted ions from some other ions class. The peak at $|1/2g\rangle \rightarrow |5/2e\rangle$ is still there and has become bigger, as expected.*

Figure 4.1: *Readout spectra for the transitions from each ground state to all excited states. The left column shows the absorption spectra for when all ions are in the desired ground state and the right column is when they should all have been removed from the ground state, thus no absorption on the original frequencies should occur. In the two lower sets the peak at 4 MHz comes from a transition from another ground state than the other peaks. Thus the 4 MHz-peak should not be visible in the left column but only in the right. Note that these are the readout spectra: the peaks are not at a correct frequency interval from each other, and the frequency is only used for reference. The reason to this is that the readout area is small (2 MHz) compared to the frequency difference between the pits (tens of MHz). The spectra could be adjusted by separating the peaks by the correct spectral distances given in figure 1.6. The spectra are taken as averages over 50 measurements. The absorption is given in αL where α is the absorption coefficient and L is the optical length.*

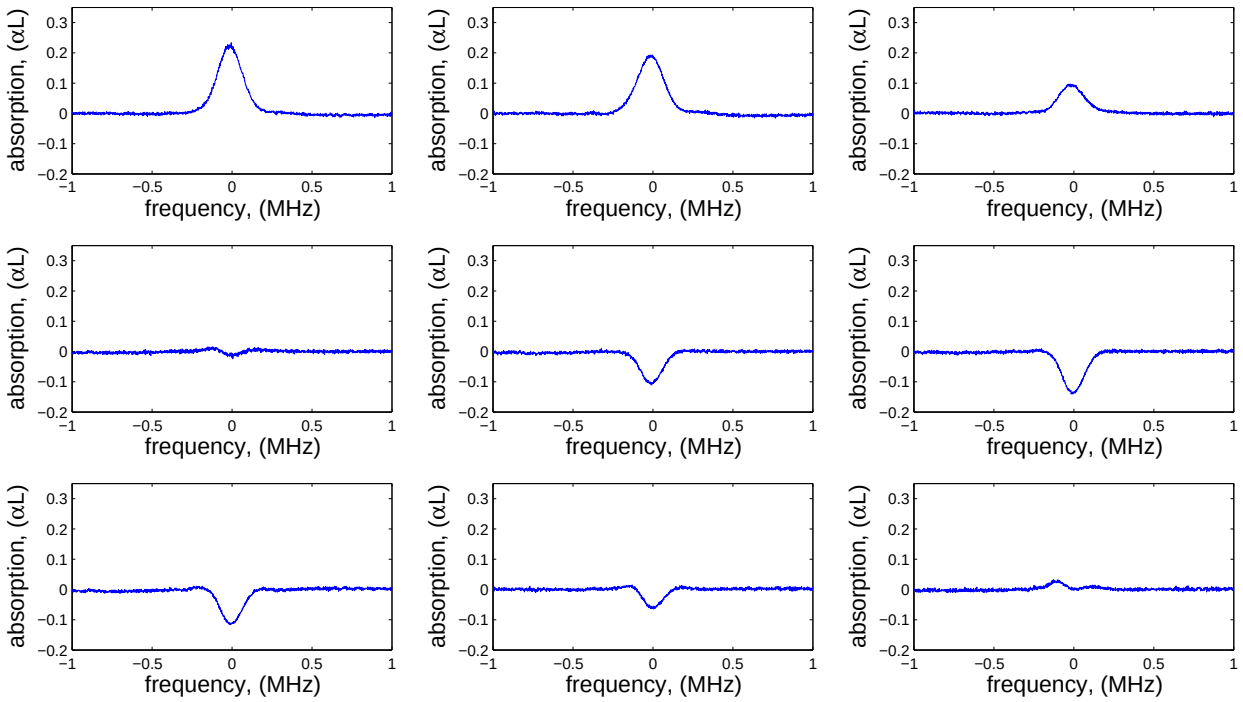

Figure 4.2: *Readout spectra for Rabi frequency measurements for the transition* $|1/2g\rangle \rightarrow |5/2e\rangle$*, using square pulses of 2* μs *and waiting 10* μs *before readout. The first plot shows the full peak. Then the Rabi frequency is increased with an equal amount each time. In the fourth plot a pulse area of* $\sim \pi/2$ *seems to have been reached, corresponding to a population of* 50% *in each state. In the sixth plot the population is almost completely inverted, and in the last plot the population is once again* $\sim$ 50% *in each state. The frequency domain only refers to the readout which was centered on the transition peak.*

The same procedure was repeated for the $|5/2g\rangle$ state, seen in figure 4.1c. In the left figure there are four peaks, of which the third at 4 MHz, corresponding to the transition $|1/2g\rangle \rightarrow |5/2e\rangle$, was not desired. This comes from an unwanted ion-class with transitions at other frequencies than the desired ion-class. It is thus not the transition $|1/2g\rangle \rightarrow |5/2e\rangle$ for the ions causing this peak. When burning at either of the two first peaks at 0 MHz and 2 MHz, these two both disappear while the fourth peak at 6 MHz becomes only somewhat smaller. The peak at 4 MHz grows bigger as it should. This is shown in the right plot in figure 4.1c.

When burning at the peak at 6 MHz all peaks but the peak at 4 MHz disappears. The peak at 4 MHz also becomes bigger than when burning on any of the two first peaks, at 0 MHz and 2 MHz. This could imply that the part left in the peak at 6 MHz in figure 4.1c is correlated to the unwanted ions in the peak at 4MHz. If so, the unwanted ions could maybe have been removed by burning at the peak at 4 MHz.

4.2 Oscillator Strengths

The readouts were done both going up and down in frequency to minimize systematical errors due to effects caused by absorption of the readout pulse. A program was used to evaluate the area under each absorption peak, which is directly proportional to the oscillator strength. The absorption spectra used for these measurements were of the same kind as those shown in figure 4.1. The evaluated areas were normalized to obtain the values presented in table 4.1.

The oscillator strengths for $^{153}Eu^{3+}$:Y_2SiO_5 at site 1, taken from reference [6], and the corresponding table with measured values for $^{151}Eu^{3+}$:Y_2SiO_5 at site 2 are shown in table 4.1. As seen, the transition strengths are not the same for the two cases but differs significantly. The transition $|1/2g\rangle \rightarrow |5/2e\rangle$ is as expected the strongest one, but the transition $|3/2g\rangle \rightarrow |5/2e\rangle$ was only about relatively half as strong as in $^{153}Eu^{3+}$:Y_2SiO_5 at site 1.

The weak transition strength means that a higher laser power is needed to obtain the same Rabi fre-

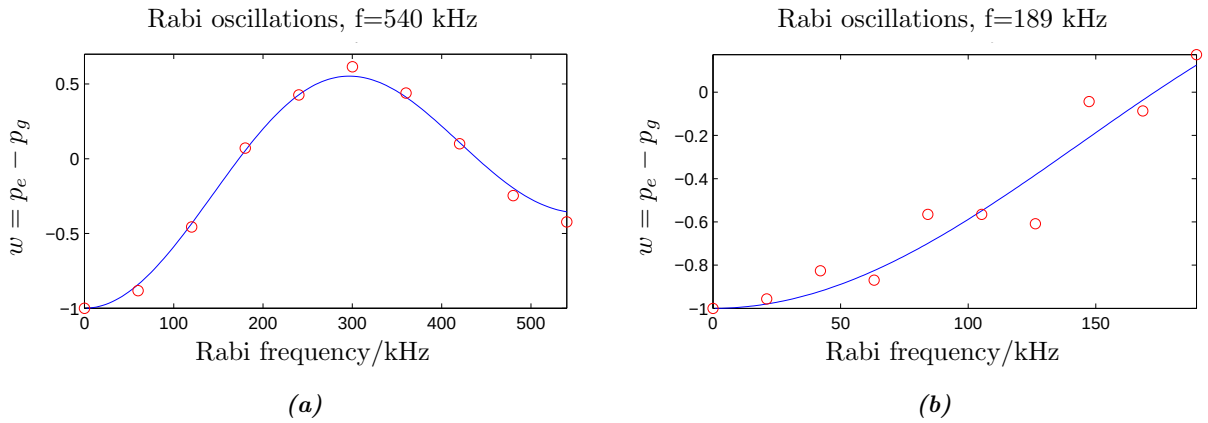

Figure 4.3: *Data fit curves for the Rabi frequency measurements of the transitions $|1/2g\rangle \rightarrow |5/2e\rangle$ in (a), and $|3/2g\rangle \rightarrow |5/2e\rangle$ in (b). These were the two transitions used for the prototype qubit. The red circles show the data points and the blue line is the fit. The rightmost data point indicates the highest achievable Rabi frequency for each transition. The Rabi frequencies stated in the figure titles and table 4.2 are given for some specified input to the AOM.*

Table 4.1: *(top) Relative oscillator strengths for $^{153}Eu^{3+}:Y_2SiO_5$ site 1. The values have an uncertainty of ±0.03 [6]. (bottom) Measured relative oscillator strengths for site 2 $^{151}Eu^{3+}:Y_2SiO_5$. Uncertainties are estimated to 0.03.*

transition	$\|\pm 1/2e\rangle$	$\|\pm 3/2e\rangle$	$\|\pm 5/2e\rangle$
$\|\pm 1/2g\rangle$	0.03	0.22	0.75
$\|\pm 3/2g\rangle$	0.12	0.68	0.20
$\|\pm 5/2g\rangle$	0.85	0.10	0.05

transition	$\|\pm 1/2e\rangle$	$\|\pm 3/2e\rangle$	$\|\pm 5/2e\rangle$
$\|\pm 1/2g\rangle$	0.01	0.11	0.88
$\|\pm 3/2g\rangle$	0.18	0.73	0.09
$\|\pm 5/2g\rangle$	0.81	0.16	0.03

quency for the weaker transition than for the stronger transition. Thus a higher laser power is also needed to create a pulse area $\theta = \pi$ for the weaker transition, which is needed for making a complete transitions from the ground state to the excited state. To achieve a larger pulse area the time of the pulse could also be increased, but this was not desired as the spontaneous decay of the ions would then become more important.

As the peak corresponding to the transition $|5/2g\rangle \rightarrow |5/2e\rangle$ did not only contain ions from the desired ion-class this peak was disregarded in the measurements (see figure 4.1c). The small value obtained from the data analysis does however corresponds well to the small change in this peak when burning at any of the other two transition from $|5/2g\rangle$.

The uncertainties in table 4.1 are estimated by comparing the individual results from each measurement for which the table is an average. There were four of these for each row/column. The largest uncertainty was 0.03, and the others ranged within 0.01-0.02.

4.3 Rabi Frequency Measurements

The purpose of measuring the Rabi frequency was to determine the correspondence between the beam intensity and the Rabi frequency experienced by the ions. These measurements were done for seven of the nine possible transitions. The two transitions $|1/2g\rangle \rightarrow |1/2e\rangle$ and $|5/2g\rangle \rightarrow |5/2e\rangle$ were not considered as the former was to weak (see figure 4.1b) and the latter contained unwanted ions (see figure 4.1c).

The Rabi frequency measurements were done by creating a pit at the transitions that was to be studied and burn the desired ions back into this pit. Only one transitions was studied at a time. Thus the measurement always started with the ions in the ground state of the current transition. In figure 4.2 the studied transitions is $|1/2g\rangle \rightarrow |5/2e\rangle$, and the system was thus initialized with all ions in $|1/2g\rangle$.

The ions were then put into a superposition state using a 2 μs square pulse, and a readout spectra was taken. At readout the ions will collapse to either

Table 4.2: *Measured maximum Rabi frequencies obtainable with the present setup for all transitions but $|1/2g\rangle \rightarrow |1/2e\rangle$ and $|5/2g\rangle \rightarrow |5/2e\rangle$, as the former was too weak and the latter contained ions from an undesired ion-class.*

transition	$\|\pm 1/2e\rangle$	$\|\pm 3/2e\rangle$	$\|\pm 5/2e\rangle$
$\|\pm 1/2g\rangle$	-	200 kHz	540 kHz
$\|\pm 3/2g\rangle$	275 kHz	495 kHz	189 kHz
$\|\pm 5/2g\rangle$	574 kHz	275 kHz	-

the ground or the excited state. Ions collapsing to the ground state will absorb the readout pulse, creating a peak in the readout spectrum. For the ions collapsing to the excited state the readout pulse will cause stimulated emission, which will cancel or reverse the absorption peak. Thus the absorption peak will shrink for increased Rabi frequency, as more will be transferred to the excited state.

The first plot in figure 4.2 shows the full absorption peak of the transition $|1/2g\rangle \rightarrow |5/2e\rangle$, that is all ions are in $|1/2g\rangle$. The ions were put into different superposition states by varying the intensity, and thus the Rabi frequency, of the 2 μs square pulse. The second plot shows the absorption peak after a relatively weak pulse. As can be seen, the peak has become smaller, as some ions has collapsed to the excited state at readout.

The third plot in figure 4.2 shows the absorption peak for a pulse with twice the Rabi frequency as used in the second plot. For the following six plots, this very same procedure was redone with the Rabi frequency successively increased an equal amount between each measurement. The system was reset between each measurement to have all ions in the ground state when the square pulse was applied.

In the fourth plot there is approximately an equal amount of ions collapsing to either state at readout. In the fifth plot more ions collapse to the excited state than to the ground state, and the peak is inverted.

As mentioned square pulses were used for these measurements, even though the sechyp pulses are more efficient for making a transfer. This is because the final superposition state is more sensitive to the Rabi frequency of a square pulse, than of a sechyp pulse.

The areas under the absorption peaks shown in figure 4.2 were evaluated and a fit was optimized to the data points, to give the Rabi frequency of the best fit. The fits for the transitions $|1/2g\rangle \rightarrow |5/2e\rangle$ and $|3/2g\rangle \rightarrow |5/2e\rangle$ which were used for the prototype qubit are shown in figure 4.3. The x-axis shows the Rabi frequency experienced by the ions and the y-axis shows the inversion, or w in the Bloch picture. The inversion was obtained by normalizing the area under each peak in figure 4.2 with respect to the initial peak when all ions are in the $|1/2g\rangle$ state.

The maximum Rabi frequency that could be obtained with the current setup, given by the fit for all considered transitions, are presented in table 4.2. Note that the presented values are rather arbitrary, and does only couple the experimental setup to the response of the ions. The absolute values in table 4.2 are not of any physical importance, but merely used to relate the beam intensity to the Rabi frequency experienced by the ions, as this was unknown before these measurements. The Rabi frequency measurements were also compared to the relative oscillator strengths. As has been mentioned previously the square root of the oscillator strengths should only differ from the Rabi frequency measurements by a constant. This is discussed in section 5.1.

The highest achievable Rabi frequency with the considered setup for the two qubit transitions are given as the highest frequencies in figures 4.3a and b: 540 kHz respectively 189 kHz. These now corresponds to the maximum beam intensity. With higher laser power, or a more efficient AOM, higher Rabi frequencies could be achieved.

4.4 Transition Fidelity

Ultimately the aim for this project was to measure the fidelity for the transitions $|1/2g\rangle \rightarrow |5/2e\rangle$ and $|3/2g\rangle \rightarrow |5/2e\rangle$, in order to investigate whether this could possibly be used for quantum computer hardware. These particular transitions were used considering the work of F. Könz et al. [4]. As has been mentioned they correspond to the transitions $|0\rangle \rightarrow |e\rangle$ and $|1\rangle \rightarrow |e\rangle$ discussed in section 1. This is illustrated in figure 1.6.

Similar experiments has been done previously using a praseodymium doped YSO crystal, with results of approximately 96% transfer efficiency for a complete transfer between the two ground states [12]. This corresponds to a single transfer efficiency of more than 97%. Due to the longer life times and narrower homogeneous linewidths in Eu higher transfer efficiencies were hoped for in this element. Unfortunately, no reliable results were obtained.

With the purpose to assure that the transfer efficiency behaved as expected, four different pulses were used for the first transfer $|1/2g\rangle \leftrightarrow |5/2e\rangle$. Only one pulse was used for the second transfer, $|3/2g\rangle \leftrightarrow |5/2e\rangle$, the pulses are presented in table 4.3.

Table 4.3: *Different pulses used for population transfer. Transfer efficiency for the first transition $|1/2g\rangle \leftrightarrow |5/2e\rangle$ was evaluated for all pulses, while only pulse 2 was used for the second transition $|3/2g\rangle \leftrightarrow |5/2e\rangle$.*

pulse	1	2	3	4
frequency/kHz	510	156	100	60
freq. FWHM	960	582	356	976
time duration/μs	5.11	60	80	206
time FWHM/μs	1.71	16.5	17.88	154

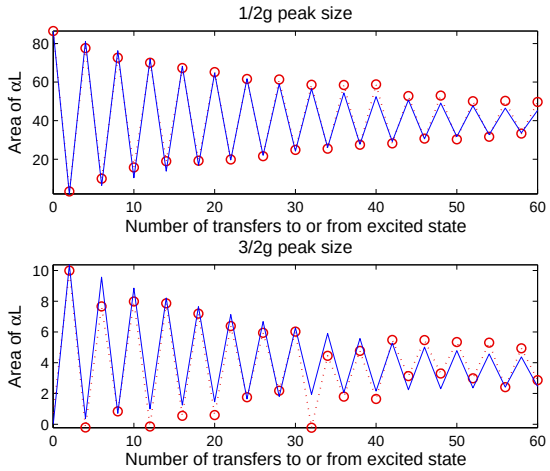

Figure 4.4: *Data from the transition fidelity measurements. The red, dotted line shows the data with the red circles indicating the data points. The blue, solid line shows the fit. The upper plot shows data for $|1/2g\rangle \leftrightarrow |5/2e\rangle$ using pulse 1 and the lower plot is for $|3/2g\rangle \leftrightarrow |5/2e\rangle$. The fit is done with the requirements from case 3 described below.*

The essential difference between the pulses is a decrease in Rabi frequency and an increase in time duration to compensate for the decrease in Rabi frequency. Pulse 1 is optimized for the transition $|1/2g\rangle \leftrightarrow |5/2e\rangle$ and pulse 2 is optimized for $|3/2g\rangle \leftrightarrow |5/2e\rangle$. Results from simulations for pulse 1 are shown in figures 2.1-2.3.

The transfer from $|1/2g\rangle$ to $|3/2g\rangle$ via the excited state was thus done using four different pulse sequences, as each of the four different pulses was used for the transfer from $|1/2g\rangle$ to the excited state, and only pulse 2 was used for the transfer from the excited state to $|3/2g\rangle$.

For each of the four pulse sequences a curve was fit to the data, minimizing four parameters: The relative

Table 4.4: *Results from making fits to the data from four different pulse sequences for making the transfers. Definitions of the different cases are described above. All numbers are given in percent.*

	pulse	$d_{1/2}$	$d_{3/2}$	$p_{1/2}$	$p_{3/2}$
Case 1	1,2	53.3	6.3	98.4	96.6
	2,2	51.0	6.5	95.4	96.0
	3,2	52.3	6.4	95.1	95.2
	4,2	49.7	6.8	89.7	94.6
Case 2	1,2	51.7	6.2	98.3	96.7
	2,2	51.7	6.2	96.0	96.2
	3,2	51.7	6.2	95.1	95.5
	4,2	51.7	6.2	90.1	94.3
Case 3	1,2	47.4	5.9	98.3	96.5
	2,2	47.4	5.9	95.5	96.5
	3,2	47.4	5.9	94.0	96.5
	4,2	47.4	5.9	87.9	96.5

decay to each of the ground states $|1/2g\rangle$ and $|3/2g\rangle$, denoted $d_{1/2}$ and $d_{3/2}$ respectively, and the transfer probability for each of the two transitions, denoted $p_{1/2}$ and $p_{3/2}$. The fit was done using three different requirements, which should optimally yield the same results:

- Case 1: All parameters were adjusted to obtain the best fit for each of the four pulse sequences separately.
- Case 2: The decay to the ground states was required to be the same regardless of the pulses used for making the transfers.
- Case 3: The decay to the ground states and the transfer probability of the $|3/2g\rangle \leftrightarrow |5/2e\rangle$, $p_{3/2}$, was required to be the same regardless of the pulse used for transfers between $|1/2g\rangle$ and $|5/2e\rangle$. As only pulse 2 was used for the former transfer, the probability should not differ between the different pulse sequences, i.e. $p_{3/2}$ should not change.

Typical plots of the collected data with fits are shown in figure 4.4. Each maximum or minimum in the plots corresponds to an average of ten data points for a number of single transfers. A single transfer is defined as a transfer between one of the ground states

and the excited state in either direction. This means that a transition between the two ground states requires two single transfers. Between each measurement the system was completely reset to the initial state, shown schematically in figure 1.8b. On the x-axis is the number of transfers and on the y-axis the area of the absorption peak in terms of αL is shown.

The results of the fit for each case are shown in table 4.4. As is seen quite different results are obtained for the different restrictions, which should not be the case. The result also depends notably on the number of included data points.

Another problem with the results are that they are all below what was expected from simulations. As best a transfer efficiency of 98.4% can have been achieved for a single transfer. This is better than the 97% efficiency of a single transfer reported in [12], but as both transitions are needed for the qubit, nothing is really gained and yet higher efficiencies are needed to create a functional qubit.

5 Curiosities, Errors and Discussion

The time for this project was too limited to draw any rigid conclusions concerning how high transition efficiency could be reached for the Eu^{3+}:Y_2SiO_5, which was the aim of the project. However, after considering parameters which are yet to be optimized, the goal of reaching an efficiency of more than 99% does not need to be out of reach. The shortcomings, potential errors and noteworthy aspects of this project will now be addressed.

5.1 The Rabi Frequency and Oscillator Strengths

In plot four and nine of figure 4.2 the absorption peak is gone, but there is still some wave-like shape in the spectrum. This is most likely because the square pulse is very frequency selective, and thus the edges of the peak does not experience the same Rabi frequency as the center of the peak. In the sixth plot in figure 4.2 the population is inverted and the absorption becomes negative due to stimulated emission.

The emission peak never becomes as big as the absorption peak. This could have several explanations. It could be due to decay: The fluorescence lifetime of the $^5D_0$ excited level at 3 K is measured to 1.62 ms [4]. About 0.5% should then have had time to fall down into the ground state before readout, which should not affect the results notably in this case. The difference is probably because the edges of the peak are not affected by the highly frequency selective square pulse. This should not have affected the results considerably, as the maximum inversion still occurs for the same beam intensity.

The square of the Rabi frequency for a transition is proportional to the oscillator strength of the transition, as the latter is proportional to the square of the dipole moment of the ion or atom. By taking the square and normalizing the Rabi frequency measurements in table 4.2 the relative oscillator strengths should thus be obtained.

An interesting thing to note is that this is not quite the case, which is realized by looking at the strongest transition for each measurement. For the Rabi frequency measurements this is not the $|1/2g\rangle \rightarrow |5/2e\rangle$ transition as would be expected from measurements of the relative oscillator strengths. By looking at ratios between the measurements in these tables the Rabi frequency deviating the most from what would be expected from the relative oscillator strengths in table 4.1 is less than 20% off, and the best values are less than 1% off.

5.2 Decay and Setup Issues

If the excited ions were to relax directly to the ground level, the relative oscillator strengths should be proportional to the decay to the different ground levels. However, the decays obtained from the fits for estimating the transfer fidelity in table 4.4 do not match the relative oscillator strength matrix in table 4.1. Table 4.1 describes the coupling for a transition from one of the hyperfine ground states to one of the hyperfine excited states relative to the other transitions between the ground and excited state. However, there are several levels between the two levels used in this experiment. Thus there is nothing that guarantees that the coupling strengths are the same from the excited stated to the ground states, as the relaxation could very well be non-trivial and occur through several steps.

To minimize errors from decay the intensity needs to be as high as possible, which was a problem in this experiment. The maximum laser output still required the duration of the pulse to be several to tenths of μs. Care was taken to maximize the laser output. The power still decreased from 1 W at the dye laser to some tenths of mW where the beam actually went through the crystal. The crystal length of 8.6 mm required a long focus for the measurements to be accurate. To keep the focus close to homogeneous throughout the crystal the beam could not be focused too hard, which also decreased the intensity.

To be able to achieve a tighter focus, and thus increase the Rabi frequency it would be desirable to use a thinner crystal. With a higher Rabi frequency the duration of the pulse could be decreased. According to simulations, larger Rabi frequency and shorter

duration did in general result in a higher transfer efficiency. The drawback of this would be a decrease in the signal to noise ratio. Due to problems with the setup and time limitations this was not done during this project.

5.3 Error Sources

As mentioned in section 4.4, the results for the transfer efficiency were consistently lower than predicted by the simulations. The population plot from pulse 1, which is the most efficient pulse, can be seen in figure 2.3. The average population transfer should be about 99.6%, and the lowest transfer considering the pinhole should be 99%. For the less efficient pulses the best result from the fit and the theoretical result differs even more.

A simple explanation to why the results did not match the simulations would be that the pinhole was set up in a way that allowed for more light to go through than was desired. In the lower right plot in figure 2.3 it is seen that the transfer efficiency decreases rapidly towards the edges of the beam. However, especially for the less efficient pulses, the error in what goes through the pinhole needs to be rather large to account for the differences between the measured and simulated transfer efficiency. Assuming the lenses and the pinhole could be some centimeter off the optimal position the radius of the beam passing through the pinhole could have approached 20 μm. This partially explains the poor results, though not completely.

The focus was measured to be 70 μm outside the cryostat. At one Rayleigh length, that is when the focus has increased to $\sqrt{2} * 70$ μm, it is 100 μm and this occurs at 7 mm from the focus point. The focus was thus within 100 μm throughout the crystal.

If the focus was assumed to be 70 μm instead of 100 μm in the simulations, the considered setup should still result in a population transfer of 99%. This does however not consider that the focus is not homogeneous throughout the beam, but will have a shape resembling a time-glass with the most narrow part in the center of the crystal. The overestimated focus used in the calculations could thus completely or partly explain the deviations in the experimental results from simulations. The crystal was also placed in a bath of liquid nitrogen at 2.17 K inside the cryostat, which could potentially have changed the properties of the focus. If the center of the focus was not in the center of the crystal, this could also have affected the outcome of the experiments.

If the pinhole also was assumed to let through light within 20 μm from the beam center instead of 16 μm, which corresponds to a displacement of some centimeter, the population transfer should be 97.9% for the most efficient pulse, (pulse 1 in table 4.3). This is less than actually obtained, and for this the time-glass shape of the focus has still not been considered.

For the less efficient pulses (pulse 2 to 4 in table 4.3) the deviations are even bigger than what is explained by the mentioned potential errors. The time was unfortunately too limited for further investigations of this. It is somewhat curious that the deviations increase for the less efficient pulses, and it implies that there is something in the setup that has not been properly considered.

5.4 Interpretation of the NOT-gate

It was mentioned in section 1 that the qubit studied in this project was supposed to work as a NOT-gate, described in section 1.1.1. In the experimental part though, only full transfers $\alpha|0\rangle \leftrightarrow \alpha|1\rangle$ has been considered. This should however not matter, as a π-pulse which completely inverts the system should be equal regardless whether the transitions is from the ground to the excited state or the reverse.

The complete operation of the NOT-gate is described in equation 1.1. The first operation inverts the populations in $|0\rangle$ and $|e\rangle$. This corresponds to the transition $|1/2g\rangle \leftrightarrow |5/2e\rangle$ which was the stronger transition, for which four different pulses were used in the experiments. The second operation inverts the population in the two states $|e\rangle$ and $|1\rangle$. This corresponds to the weaker transitions in the experiments, which was $|5/2e\rangle \leftrightarrow |3/2g\rangle$. The third and last operation inverts the population between the states $|e\rangle$ and $|0\rangle$. This would correspond to the transition $|5/2e\rangle \leftrightarrow |1/2g\rangle$. However, as there were no ions in $|3/2g\rangle$ to start with, there would after the two first operations be no population left in $|5/2e\rangle$, and thus this last operation was unnecessary for the transition $|1/2e\rangle \rightarrow |3/2g\rangle$.

By simply adding a pulse corresponding to the third inversion in equation 1.1 the created qubit would completely invert any superposition state $\alpha|0\rangle + \beta|1\rangle$. The same argumentation applies for the reversed transfer $|3/2g\rangle \rightarrow |5/2e\rangle \rightarrow |1/2g\rangle$ in the experiments, with the difference that there is now no need for the first operation in equation 1.1, as both $|1/2g\rangle$ and $|5/2e\rangle$ are initially empty.

6 Conclusions and Outlook

The goal of the project was to acquire a transfer efficiency of at least 99% for a specific transition in the Eu ions in $^{151}Eu^{3+}$:Y_2SiO_5. This goal was un-

fortunately not fulfilled due to reasons discussed in section 5, but at most a transfer efficiency of 98.4% can have been achieved. Together with a possible maximum transfer efficiency of 96.6% of the weaker transfer, this would results in a double transfer efficiency of at most 95%, which can be compared to the 96% achieved for the $Pr:Y_2SiO_5$ crystal mentioned in section 4.4 [12].

The measured transfer efficiency was consistently lower than expected from simulations. This could partially or completely be explained by misplaced optics and a smaller focus than what was used in the simulations. For the less efficient pulses the deviations from simulations were bigger than for the most efficient pulse. The deviations for the most efficient pulse could be completely explained with the mentioned error sources. This is however not the case for the less efficient pulses, for which the results could only be partially explained by the mentioned error sources.

The possibility to reach 99% transfer efficiency for the single transfer is thus still not necessarily out of reach, but more care needs to be taken in the selection of what part of the beam is considered at readout by choosing a smaller pinhole. To improve the simulations and gain better understanding for the properties of the focus the fact that this is not homogeneous throughout the beam could be implemented into the program.

Other improvement that could be made is adding an external magnetic field to prevent spin flips in the crystal which would further increase the coherence time, and a thinner crystal could be used to achieve a higher Rabi frequency. The properties of the focus inside the cryostat chamber should also be more rigorously investigated.

It is though not enough to gain 99% efficiency for only one of the transfers, as a complete qubit operation involves both transfers. To achieve a total transfer of 99% higher transfer efficiency are thus required also for the weaker transition. However, if the Rabi frequency is increased for one of the transitions it will most likely be increased for both transitions, as it is proportional to the electric field of the laser beam. The limiting factor is mainly the Rabi frequency, and the most efficient way for obtaining better results is probably to use a laser with higher output.

References

[1] Mattias Nilsson. *Coherent Interactions in Rare-Earth-Ion-Doped Crystals for Applications in Quantum Information Science*. PhD thesis, Deparment of Physics, Lund Institute of Technology, 2004.

[2] David Deutsch. Quantum theory, the church-turing principle and the universal quantum computer. *Proceedings of the Royal Society of London A*, 1985.

[3] David Deutsch and Richard Jozsa. Rapid solution of problems by quantum computation. *Proceedings of the Royal Society*, 1992.

[4] F. Könz et al. Temperature and concentration dependence of optical dephasing, spectral-hole lifetime, and anisotropic absorption in Eu^{3+}:Y_2SiO_5. *Physical Review*, 2003.

[5] R. J. Elliott. Theory of nuclear magnetic resonance in Eu^{3+}, 1957.

[6] B. Lauritzen et al. Spectroscopic investigations of Eu^{3+}:Y_2SiO_5 for quantum memory applications. *Physical Review B 85*, 2012.

[7] Y. C. Sun. *Rare Earth Materials in Optical Storage and Data Processing Applications*. Springer, 2005.

[8] R. W. Equall, Y. Sun, R. L. Cone, and R. M. Macfarlane. Ultraslow optical dephasing in Eu^{3+}:Y_2SiO_5. *Physical Review Letters*, 1994.

[9] Ingela Roos and Klaus Mølmer. Quantum computing with an inhomogeneously broadened ensemble of ions: Suppression of errors and coherent population trapping. *Physical Review A 69*, 2004.

[10] R.W.P Drever et al. Laser phase and frequency stabilization using an optical resonator. *Applied Physics B*, 1983.

[11] Lars Rippe. *Quantum computing with naturally trapped sub-nanometre-spaced ions*. PhD thesis, Deparment of Physics, Lund Institute of Technology, 2006.

[12] A. Walther Y. Ying L. Rippe, B. Julsgaard and S. Kröll. Experimental quantum-state tomography of a solid-state qubit. *Physical Review*, 2008.